Photocatalytic H_2 Production from Microplastics Containing Shower Gels and Personal Care Products with Cobalt Oxide Nanocomposite

DELİA TERESA SPONZA, RUKİYE ÖZTEKİN*
Department of Environmental Engineering
Dokuz Eylül University
Tınaztepe Campus, 35160 Buca/Izmir,
TURKEY

*Corresponding Author

Abstract: - Microplastics (MPs) pose a significant threat to human health, primarily through their entry into the food chain through the consumption of contaminated fish. Additionally certain personal care products including shower gels, face cleansers, hand gels, detergents, tootphasete and creams are recognized as potential sources of microplastic pollution due to presence of polymers like polyethylene and polystyrene. In the present study, cobalt oxide (Co_3O_4) nanocomposites (NCs) were synthesized and employed as photocatalysts for hydrogen production under solar simulated conditions from microplastics namely Polyamide (PA, Nylon), Polyacrylate (PAR), Polyethylene (PE), Polymethyl methacrylate (PMMA) and Acrylates Copolymer (AC). The aforementioned nanocomposite was utilized to degrade some microplastics extracted from shower gels and facial creams for hydrogen (gas) generation. The Co_3O_4 nanocomposites were generated in controlled laboratory conditions. The structural, morphologic and, surface characteristics of the nanocomposite were characterized using XRD, SEM, FTIR, HRTEM, EDX and UV-vis absorption spectrum analysis. The influence of some operational parameters including photodegradation time, and Co_3O_4 nanocomposite concentrations on H_2 efficiency from PA, PAR, PE, PMMA and AC microplastics were investigated. The maximal H_2 productions were detected as 180 mmol/g Co_3O_4 NP.h, for PE; 108 mmol/g Co_3O_4 NP.h for PAK and 105 mmol/g Co_3O_4 NP.h, for PA at 100 mg/l PE, PAK and PA microplastic concentrations, respectively, after 0.40 h retention time at 2 mg/l Co_3O_4 NPs concentrations. The maximal H_2 productions were found to be slightly low in PMMA (82 mmol/g Co_3O_4 NP.h and AC (87 mmol/g Co_3O_4 NP.h) after 0.4 h at 2 mg/l Co_3O_4 NPs at initial 100 mg/l PMMA and AC microplastic concentrations. XRD analysis confirms whether the Co_3O_4 catalyst is in the spinel phase with crystallite size. The SEM investigation revealed that Co_3O_4 NPs has small particles shaped distribution and with interconnected agglomerated particles. The average particle size of Co_3O_4 NPs was less than 15 nm. In our study, the surface area of Co_3O_4 NPs were measured as 82 m^2/g, indicating more contact points in large surface resulting in more H_2 production with Brunauer–Emmett–Teller (BET) analysis. Peaks are typically around 0.7 keV (L_α) and 6.9 keV (K_α)- for Co, and around 0.5 keV for O_2. The band gap energy around 2.35 eV provides sufficient force for the decomposition of the microplastics mentioned above. The main FTIR spectrum values are 1145 cm^{-1}, 1397 cm^{-1}, 1645 cm^{-1} and 3500 cm^{-1} for C=O, O-H, C=O and O-H bonds, respectively. The specific geometric forms of Co_3O_4 NPs, such as cubes, rods, or plates, were in the range of 10 and 50 nm and are visualized in HRTEM graphs. The maximal H_2 productions were detected as 180 mmol/g Co_3O_4 NP.h, for PE; 108 mmol/g Co_3O_4 NP.h for PAK and 105 mmol/g Co_3O_4 NP.h, for PA at 100 mg/l PE, PAK and PA microplastic concentrations, respectively, after 0.40 h retention time at 2 mg/l Co_3O_4 NPs concentrations. The maximal H_2 productions were found to be slightly low in PMMA (82 mmol/g Co_3O_4 NP.h and AC (87 mmol/g Co_3O_4 NP.h) after 0.4 h at 2 mg/l Co_3O_4 NPs at initial 100 mg/l PMMA and AC microplastic concentrations. The reusability studies showed that the Co_3O_4 NPs nanocomposites exhibited the same H_2 productions for 64 cycle and these nanoparticles possessed slightly improved photocatalytic degradation of microplastics.

Key-Words: - Acrylates Copolymer (AC); Cobalt oxide (Co_3O_4) nanocomposites; Hydrogen (H_2) production; Microplastics; Pharmaceuticals and personal care products (PPCPs); Photocatalytic degradation; Polyamide (PA, Nylon); Polyacrylate (PAR); Polyethylene (PE); Polymethyl methacrylate (PMMA).

Received: June 16, 2025. Revised: August 24, 2025. Accepted: September 29, 2025. Published: May 11, 2026.

1 Introduction

Pharmaceuticals and personal care products (PPCPs) originated from different class of emerging contaminants characterized by molecular weights ranging from 130 to 1400 Daltons (DA) and a wide array of physicochemical properties, [1], [2], [3].

Global consumption of PPCPs has escalated significantly over the past decade, particularly in rapidly developed economies such as Brazil and South Africa, [4], [5]. Currently, over 3000 PPCPs have been identified in the environment, largely since inefficient treatment by conventional wastewater treatment plants. These facilities are typically unable to fully degrade PPCPs, resulting in their persistent presence in aquatic systems, [6], [7], such as lakes, [8], [9], rivers, [10], ground water, [11], [12], [13], marine environments and even in drinking water, [14], [15], and in drinking water, [16], wastewater containing a mix of pharmaceuticals caused significant reproductive and other health impacts for fish, [17], [18]. Moreover, PPCPs (e.g., acetaminophen, caffeine, 1,7-Dimethylxanthine, dehydronifedine, tetracycline, oxytetracycline, sulfonamides, macrolides, and ormetoprim) have been detected in fruits, vegetables, fish, meat and milk due to uptake from an environment contaminated by PPCPs, [13], [19], [20], [21]. Innovative solutions, such as advanced remediation processes, should be taken into account to minimize the emissions of PPCPs into environment. Photodegradation can be accepted as a sustainable process.

Innovative and efficient treatment technologies are urgent required to mitigate the environmental dissemination of PPCPs. Among these, heterogenous photocatalysis has emerged as a promising sustainable alternative. Heterogeneous photocatalysis is an advanced oxidation process that utilizes semiconductor materials activated by light to generate electron-hole pairs, initiating redox reactions on their surfaces. Electrons, and holes on the surface of a semiconductor participate in redox reactions that produce reactive species such as hydroxyl radicals ($OH^{\bullet}$) and superoxide anion radicals ($O^{-2\,\bullet}$).

MPs can be used extensively in personal care products (PCPs) containing powders, concealers, eye shadows, eye pencils, eyeliners, deodorants, sun care, hair care like conditioners and dry shampoos. Although, shower gels and personal care products are used more frequently than other microplastics, and they could easily emit and has high durability, by increasing the disturbances of toxic chemicals. These compounds also bioaccumulated and transferred into the food chain in marine environments, [22], [23], [24]. Polyamide (PA, Nylon), PA), Polymethyl methacrylate (PMMA), Polyethylene (PE) and Acrylates Copolymer (AC) are microplastics present in the structure of shower gels and personal care products.

Polyamide (PA, Nylon) is a polymer with repeating units connected by amide bonds. The chemical structure of PA MPs was shown in Fig. (1a). Polyamides are found in nature, both naturally and synthetically. The most well-known examples of natural polyamides are natural PA forms containing proteins, such as wool and silk. Artificially produced synthetic polyamides are produced by the step-growth polymerization method or by solid phase synthesis, and are obtained as materials such as nylons, aramids and sodium polyaspartates. Synthetic polyamides are widely used in the textile and automotive industry, carpets, kitchenware and sportswear thanks to their significant advantages such as high durability and strength. The transportation and manufacturing industry are among the main consumer activities that account for a significant portion of PA consumption.

* Figure 1 can be found in the Appendix section.

In addition to, the composition of their main chain, synthetic polyamides are classified as: Aliphatic Polyamides, Semi-aromatic Polyamides, and Aromatic Polyamides, respectively. All polyamides are formed by an amide chemical reaction that bonds two monomer molecules together. The amides can be α,ω-amino acids, and usually are the form of a cyclic lactam such. These two types of precursors form a homopolymer. Polyamides copolymerize readily, and this occurs with a large number of monomer mixtures that can form a large number of copolymers. However, many nylon polymers are miscible with each other, which is a significant advantage that enables the creation of new nylon polymer blends.

In polymer generation, two groups produce an amide bond. This process involves amide bonds, with an amine moiety and the terminal carbonyl moieties of the relevant group. These mix to produce a carbon-nitrogen group to form amides. This polymerization occurs with emission of other atoms. The carbonyl component is assumed to be part of a carboxylic acid group or a more reactive acyl halide derivative. The chemical structures of the most widely used types of nylon polymers produced synthetically in the industry, namely PA, Nylon 6 (Fig. 1b) and PA, Nylon 66 (Fig. 1c), are given in detail. Condensation reactions; It is thought to indicate that in living organisms, for example, amino acids condense with each other to form amide bonds (and/or peptides) by an enzyme. The polyamides that emerge after condensation reactions are known as proteins or polypeptides. According to the assumption that the difference between Radical (R) groups is negligible; Replacement Radical groups are ignored. Polyamides; It can also be synthesized from dinitriles using acid catalysis, as an application of the Ritter reaction, [25], [26].

Polyacrylate (PAK) MPs, an acrylate polymer (also known as acrylic), represents any of a group of polymers prepared from acrylate monomers, [27]. The general chemical structure of PAK MPs is described in detail in Fig. 2. The most important advantages of PAK plastics are their transparency and resistant to breakage and have high elasticity. Acrylate polymer is used as an adhesive in cosmetic products such as nail polish.

* Figure 2 can be found in the Appendix section.

Acrylic elastomer has high heat and oil resistance properties; and can withstand temperatures up to 170-180°C. Acrylic elastomer is used especially in the production of oil seals and packaging related to automobiles, [28]. Acrylic elastomer is generally defined as one of two types. The "old" type of acrylic elastomers includes the chlorine-containing ACM (acrylic acid ester and 2-chloroethyl vinyl ether copolymer) as well as the chloride-free ANM (acrylic acid ester and acrylonitrile copolymer). The most important advantages of the "new" type of acrylic elastomers are that they do not contain chlorine and are more resistant to staining caused by mold.

The most important disadvantages of the new type of acrylic elastomers are that their rebound flexibility and wear resistance are poor, and even their electrical properties are much weaker than those of acrylonitrile-butadiene rubber and butyl rubber. The most important areas of use of PAK MPs can be listed as follows: As a binder in polyacrylate emulsion, water-based coating and exterior and interior "latex" house paints, acrylic paints as artist paints, and acrylic fibers, etc. In addition, Sodium polyacrylate: water-soluble thickeners, is a polymer used as a raw material in the production of Super Absorbent Polymer (SAP), used in disposable diapers, due to its high absorbency per unit mass. Some other areas of use for PAK MPs include; It is also used in acrylic resins as a pressure sensitive adhesive, and as a formulation of cyanoacrylate used as a raw material in the production of "Super Glue". Other areas of use of PAK MPs include; PAK MPs are used as raw materials, in cosmetic, and found in the composition of acrylic acid liquids.

Polyethylene (PE) MPs [also known by their IUPAC names polythene or poly(methylene)] is extensively produced. The general chemical structure of Polyethylene (PE) MPs is described in detail in Fig. 3. It is a major polymer used in packaging and containers. Low density PE (LDPE) MPs or high-density PE (HDPE) MPs, were the group of PE MPs.

* Figure 3 can be found in the Appendix section.

All forms of PE MPs are non-toxic and chemically more stable, which contributes greatly to the widespread use of PE MPs as ergonomic plastics, [29]. LDPE MPs are softer than HDPE MPs, and much more durable. For Medium-density Polyethylene (MDPE) MPs and HDPE MPs the melting point is typically in the range 120ºC to 130°C. The melting point for average commercial LDPE MPs is typically 105ºC to 115°C. These temperatures vary greatly depending on the type of PE MPs, but the theoretical upper melting limit of PE MPs is reported to be 144ºC to 146°C, [30], [31]. Combustion typically occurs above 349°C. Most LDPE MPs, MDPE MPs, and HDPE MPs grades have excellent chemical resistance. PE MPs was dissolved at high temperatures, [30]. Some of the most important advantages of PE MPs are given below: PE MPs absorbs almost no water. Its permeability to water vapor and polar gases is lower than most plastics. In addition to, it can easily pass non-polar gases such as oxygen gas [$O_2(g)$], carbon dioxide [$CO_2(g)$] and sweeteners. PE MPs burn slowly with a blue flame with a yellow tip, and give off a paraffin odor PE MPs material continues to burn after the flame source is removed, producing a drip. PE MPs cannot be printed and/or bonded with adhesives without pretreatment. High strength connections can easily be achieved with plastic welding. PE MPs offers good electrical resistance, [31], [32], [33].

Polymerization of ethylene to PE MPs was illustrated with equation, [33], in Eq. (1):

$$nCH_2 = CH_2\,(g) \rightarrow \lfloor - CH_2 - CH_2 - \rfloor_n\,(solid) \quad (1)$$

$$\Delta H/_n = -25.71 \pm 0.59\ kcal/mol (= -107.6 \pm 2.5\ kj/mol)$$

The widespread use of PE MPs poses potential challenges in terms of “waste management” because it does not readily biodegrade. Japan has been increasing plastic recycling since 2008; however, according to 2008 data, there were still reports of large amounts of plastic packaging waste going to waste, [34]. They are high number experimental studies on the biodegradability of PE MPs, some of these experimental studies are summarized below: Some enzyme or bacteria can minerilase the PE MPs. Many plastics (polyesters, polyamides) can be degraded by hydrolysis. Degradation by bacteria with enzyme degrade the PE MPs, [35,36].

Polymethyl Methacrylate (PMMA) MPs [The full IUPAC chemical name is poly(methyl 2-methylpropenoate or also known as Poly(methyl methacrylate) and polymethylmethacrylate] is a polymer produced from methyl methacrylate. The general chemical structure of PMMA MPs was seen in Fig. 4.

* Figure 4 can be found in the Appendix section.

PMMA MPs can also be used as a casting resin, in inks and coatings, and for many other purposes. PMMA MPs is often technically classified as a type of glass, in that it is a non-crystalline vitreous substance. It's density is 1.18–1.22 g/cm^3, [37], PMMA MPs also has good impact strength, higher than both glass and polystyrene, [38]. It filters ultraviolet (UV) light at wavelengths below about 300 nm. PMMA MPs swells and dissolves in many organic solvents; it also has poor resistance to many other chemicals due to its easily hydrolyzed ester groups. Nevertheless, its environmental stability is superior to most other plastics such as polystyrene and polyethylene, and therefore it is often the material of choice for outdoor applications, [39]. PMMA MPs has a maximum water absorption ratio of 0.3–0.4% by weight. Tensile strength decreases with increased water absorption, [39]. Its coefficient of thermal expansion is relatively high at (5–10) × 10^{-5} °C^{-1}, [40].

Methacrylate polymers are used extensively in medical and dental applications where purity and stability are critical to performance, [41], [42], [43]. Acrylates (IUPAC name: prop-2-enoates) are the salts, esters, and conjugate bases of acrylic acid. The acrylate ion is the anion $CH_2=CHCO-2$. The general chemical structure of Acrylates Copolymer (AC) MPs was given in Fig.5, [44].

* Figure 5 can be found in the Appendix section.

Acrylates generated with acrylic acid with alcohol in presence of a catalyst. The reaction with lower alcohols (methanol, ethanol) takes place at between 100°C and 120°C with catalysts, [45]. Acrylate monomers are used to form acrylate polymers. Most commonly, these polymers are in fact copolymers, being derived from two monomers, [45], [46]. An acrylate polymer is any of a group of polymers prepared from acrylate monomers. These plastics are noted for their transparency, resistance to breakage, and elasticity. Acrylate polymer is commonly used in cosmetics, such as nail polish, as an adhesive,[47].

The electro-oxidation of PMMA on Pt-based electrodes in a Polymer Electrolyte Membrane (PEM) electrolyzer at 90°C was performed, [48], [49]. Polyethylene terephthalate (PET) can be degrading to H_2 via TiO_2, [50]. Co_3O_4-TiO_2 nanocomposite exhibited an aggregated shape with high surface area for treating sulphide wastewater at a sun light irradiance of 770 W/m^2, an enhanced H_2 production efficiency, [51].

It is important to use the renewable energy resources due to the environmental limitations of fossil fuel sources. Hydrogen (H_2) was extensively used as a clean energy, [52], [53]. The production of photo-catalytically H_2(g) has garnered significant attention due to its environmentally friendly nature, simple processing, ease of production and low-cost procedure. [54], [55]. Therefore, the development of technologies for H_2 production is crucial. Various metal oxides including titanium dioxide (TiO_2), ZnO, NiO and Co_3O_4 have been explored for their photocatalytic evolution capabilities, [56].

Among them, cobalt-based catalysts, particularly Co_3O_4 have garnered attention due to their unique physicochemical properties, including high stability, visible light absorption, and excellent redox activity, [57]. The spinel structure of Co_3O_4 comprises Co^{+2} and Co^{+3} ions arranged in tetrahedral and octahedral sites, contributing to its catalytic efficiency, [58]. Numerous synthesis methods, such as hydrothermal, sol-gel, precipitation and thermal decomposition, have been employed for the fabrication of Co_3O_4 nanoparticles, [58], [59]. Its exceptional magnetic, catalytic, and optical properties make it suitable for diverse applications, [60], [61], [62], [63]. Recently, researchers have investigated its potential for photocatalytic hydrogen production and crystal violet dye degradation, [64]. There are various ways to produce Co_3O_4, such as hydrothermal, sol-gel, precipitation techniques, and thermal decomposition methods, [65]. The frequently utilized technique is the high-temperature decomposition of cobalt oxalate, which involves breaking down the precursor material production, [66].

In the studies mentioned above relevant to H_2(g) production from plastic wastes exhibited low yields. Therefore, in this study, it was aimed to photodegrade the microplastics namely Polyamide (PA, Nylon) Polyacrylate (PA), Polymethyl methacrylate (PMMA), Polyethylene and Acrylates Copolymers isolated from the shower gels and personal care products like skin care products include cleansers, moisturizers, sunscreen, tonics, lotions, and serums, by generating Co_3O_4 nanocomposites. The physicochemical properties of this nanocomposite were characterized using XRD, SEM, FTIR, HRTEM, EDX and UV-vis absorption spectrum analysis. The effects of increasing Co_3O_4 nanocomposite concentrations and time on the H_2(g) productions from the aforementioned microplastics was researched. Furthermore, the reusability of the Co_3O_4 nanocomposite was investigated.

2 Materials and Methods

2.1 Generation of Co_3O_4 NPs

Cobalt nitrate hexahydrate ($Co(NO_3)_2.6H_2O$) and triethanolamine were mixed to generate Co_3O_4 by precipitation method, [51]. 4.8 mmol of $Co(NO_3)_2.6H_2O$ was dissolved in 40 ml of distilled water. 2.9 mmol of NaOH was dissolved in 40 ml distilled water. This NaOH solution was then added to the solution of $Co(NO_3)_2.6H_2O$ and reaction mixture was stirred for 4 h. The precipitate was collected and dried in an incubator at 90°C for 10 h. This sample was calcinated at 400°C for 4 h to obtain the Co_3O_4 NPs.

2.2 H_2(g) Generation

Photocatalytic studies were performed in a quartz reactor with a volume of 2 liter. Certain amount of Co_3O_4 NPs was dissolved in 130 ml of aqueous Polyamide (PA, Nylon) Polyacrylate (PA) and Polymethyl methacrylate (PMMA), Polyethylene (PE) and Acrylates Copolymer (AC) solutions, separately, containing 1, 2, 3 and 4 mg/l Co_3O_4 NPs concentrations. All microplastic concentrations were kept constant at 100 mg/l. Then, the inner of the reactor was purged of air by infusing nitrogen [N_2(g)] during 40 minutes. Once the air had been removed, a 300 W Xenon lamp with a 460 nm wavelength was used to irradiate the reactor. To prevent thermal catalysis, water was circulated through the outer layer of the reactor.

2.3 Measurement of Hydrogen

Hydrogen concentration was measured using micro-GC. Nitrogen is used as a standard carrier gas for micro-GC. The measured flow rate can vary from around 43 ml/min to around 700 ml/min in steam gasification. Molecular sieve columns allow the separation of N_2, CH_4, O_2, H_2, CO_2, and other light hydrocarbons. Molecular sieve columns type 6 A or 0.6 nm (MS-5A), by using argon as a carrier gas, are suitable for H_2, CH_4, and CO analysis at 99°C. Porapak Q (PPQ) or PoraPLOT U columns, using helium as the carrier gas, are suitable for CO_2, C_2H_4, and C_2H_6 analysis at 60 °C gas chromatography.

2.4 Physicochemical Properties

To detect the XRD patterns, a Rigakupowder X-ray diffractometer (XRD) from Japan was used. The prepared materials were examined using a Zeiss microscope to detect the scanning electron microscopic (SEM) images. Agilent CaryInstrument was used to record ultraviolet-visible (UV-vis) spectra. Energy dispersive X-ray spectroscopic (EDX) studies were conducted using an Oxford EDX instrument connected to SEM. The Fourier transform infrared spectroscopy (FTIR) spectra of samples was recorded using the FT-NIR spectroscope (RAYLEIGH, WQF-510). The dry samples on the Cu grid were viewed and examined by High resolution transmission electron microscopy (HRTEM) analysis recorded in a JEOL JEM 2100F, Japan under 200 kV accelerating voltage.

3 Results and Discussions

3.1 XRD Analysis Results

The Co_3O_4 NPs were investigated using XRD analysis within a 2θ range of 6–120° (Fig. 6). The XRD pathways of the Co_3O_4 NPs exhibited certain diffraction peaks between 6–120° 2θ, corresponding to the (224), (317), (408), (518), and (449) diffraction planes of Co_3O_4 NPs, as mentioned by the JCPDS number of 48–1480.These data exhibited that the Co_3O_4 NPs were generated with excellent phase purity.

* Figure 6 can be found in the Appendix section.

The mean crystallite size of the Co_3O_4 NPs was determined using the Debye-Scherrer equation in Eq. (2):

$$D = {k\lambda}/{\beta \cos\theta} \qquad (2)$$

Where, D is the average crystallite size in nm, β is the full width at half maximum of the observed peak, λ is theX-ray wavelength (0.161 nm) and θ is diffraction angle, Bragg angle). The morphological characteristics of the photocatalysts very important. In this connection, it is required to examine surfacestructural features of the prepared sample.

The average crystallite size (D) of Co_3O_4 NPs in this study were between 35 nm and 40 nm, depending on the synthesis method and calcination temperature. In this study, D values were measured between 6 and 38 nm while the average particle size of Co_3O_4 NPs was less than 15 nm.

Commonly D values for Co_3O_4 NPs diameters varıed between 13 and 21 nm when the nanocomcosıte generation methods were sonication and sol–gel methods, [65]. The D values were between 27 and 32 nm after calcination at 400°C, [66]. The D values were between 3 and 10 nm for Co_3O_4 NPs supported on substrates like carbon and silica and in binary nanocomposites like Co_3O_4 /MnO_2, [65].

In the production of photocatalytic H_2 gas with Co_3O_4 NPs, XRD analysis is a critical tool for determining the crystal structure, purity, and active site content of the catalyst, [65], [66], [67]. The analysis results are generally interpreted under the following headings:

When examining the XRD pattern for Co_3O_4, characteristic peaks belonging to a face-centered cubic (*fcc*) spinel structure are typically sought, [68], [69].
(a) In the literature (JCPDS card no. 42-1467 or 073-1701), 2θ values around 19.0°, 31.3°, 36.9°, 44.8°, 59.4°, and 65.3° represent crystal planes (111), (220), (311), (400), (511), and (540), respectively.
(b) The absence of other peaks (e.g., CoO or metallic Co) on the pattern besides these peaks proves that the catalyst is in the pure Co_3O_4 phase and that the synthesis process was successful.

The width of the XRD peaks directly provides information about the crystal size of the nanoparticles, [70], [71]. The characteristic peaks for cubic Co_3O_4 NPs are usually found at the following approximate 2θ positions: 18.9°–19.4°: (111) plane, 31.1°–31.3°: (220) plane, 36.7°–36.8°: (311) plane, 38.2°–38.5°: (222) plane, 44.7°–44.8°: (400) plane, 55.5°–55.7°: (422) plane, 59.3°–59.4°: (511) plane, 65.2°–65.3°: (440) plane and 77.3°–77.7°: (533) plane, respectively. (a) The wider the peaks (Full Width at Half Maximum - FWHM), the smaller the crystallite size. (b) The Debye-Scherrer equation as shown in Eq. (2). In photocatalytic H_2 production, small size (high FWHM) is preferred because it means a larger surface area and therefore more active centers. In this study, D values were measured between 6 and 38 nm. The average particle size of Co_3O_4 NPs was less than 15 nm.

Key parameters for Co_3O_4 NPs were (a) Crystal system with cubic spinel as space group namely Fd3m. (b) Lattice Constant (a) is ≈ 8.08–8.13 Å. (c) Dislocation density (δ) is typically 11.057 x 10^{14} m^{-2} for pure samples while decrease in composite forms. (d) Band gap (E_g) between 1.4–2.78 eV, indicates good photocatalytic properties.

Structural stresses affecting H_2 production efficiency can be inferred from XRD data using Williamson-Hall (W-H) analysis, [72]: Slight shifts or distortions in the position of peaks indicate the micro-strain in the crystal lattice. The presence of defects in the structure can sometimes increase the H_2 production rate by facilitating the dissociation of photoexcited charge carriers in electron-holes.

Verification of Composite Structures of Co_3O_4 by combining with materials such as ZnO or $g\text{-}C_3N_4$ increase the H_2 yields, [73]. (a) The presence of peaks for both components (e.g., a 27.5° peak for $g\text{-}C_3N_4$ and Co_3O_4 peaks) in the XRD pattern indicates successful composite formation and homogeneous mixing of the phases. (b) As the Co_3O_4 loading rate increases, the intensity of its peaks increases until an optimum level, by providing data for catalyst optimization.

In summary, XRD analysis confirms whether the Co_3O_4 catalyst is in the spinel phase, by providing insight into the surface area by calculating the crystallite size, and verifies heterojunction structures formed with other materials.

3.2 SEM Analysis Results

The SEM images were generated to analyse the topological and surface properties of Co_3O_4 NPs. The recorded SEM results for Co_3O_4 NPs are presented in Fig. 7a and Fig. 7b. The SEM investigation revealed that Co_3O_4 NPs has a small particles shaped distribution and with interconnected agglomerated particles (Fig. 7b). The average particle size of Co_3O_4 NPs was less than 15 nm (Fig. 7b).

* Figure 7 can be found in the Appendix section.

The SEM investigation revealed that Co_3O_4 NPs has a small particles shaped distribution and with interconnected agglomerated particles. The average particle size of Co_3O_4 NPs was less than 15 nm (Fig. 7c and Fig. 7d).

SEM analyses are used to elucidate the direct relationship between the material's morphology, particle size, surface area, and dispersion properties and its catalytic performance, [74], [75], [76]. The size of the majority of the Co_3O_4 NPs measured are less than 15 nm with a pore diameter of 12.77 nm, and consist of a mixture of partially and fully developed hollow spheres, with average wall thickness of 0.5–2 μm. Fig. 8 shows the Brunauer–Emmett–Teller (BET) surface area, pore size volume distribution of Co_3O_4 NPs. All powders show a narrow Gaussian distribution from 14 to 16 nm that supports SEM observations.

* Figure 8 can be found in the Appendix section.

The surface area of Co_3O_4 NPs were measured as 82 m^2/g. The higher surface area measured in Co_3O_4 NPs is explained by theadditional gases given off during processing that have resulted in anaerated powder product.

Co_3O_4 structures are in spherical, porous sheet, rod (nanorod), or flower-like (nanoflower) forms, The surface area exhibited articularly "spongy" or "hollow sheet" morphologies imply a larger specific surface area and more active sites, which increases H_2 production efficiency.Typical Co_3O_4 NPs are generally observed to have sizes ranging from 13 nm to 16 nm as reported by Li et al., [74]. The small particle size reduces the risk of recombination (characterization) by shortening the electron transfer distance to the surface. The formation of clusters of particles clinging to each other in the images is generally noted as a limiting factor in H_2 production rate, as it can reduce the effective surface area, [77, 78]. The presence of Co and O peaks confirms the chemical accuracy of the structure, [79]. In the study performed by Mohammed et al., [80], BET method revealed that Co_3O_4 NPs have a specific surface area of 14.34 m^2/g, a pore diameter of 18.94 nm, and a total pore volume of 0.034 cm^3/g, [80]. In our study, the surface area of Co_3O_4 NPs were measured as 82 m^2/g, indicating more contact points in large surface with ligth and microplastics resulting in more H_2 production with BET method.

3.3 EDX Analysis Results

The phase purity can be further determined by using EDX spectroscopy. Therefore, EDX spectrum of Co_3O_4 NPs was also obtained (Fig. 9). The obtained EDX spectrum of Co_3O_4 NPs has been presented in Fig. 9a which is showing the presence of Co and O elements (Fig. 9b). The EDX analysis revealed the successful formation of Co_3O_4 NPs with decent phase purity.

* Figure 9 can be found in the Appendix section.

In the studies on the production of photocatalytic hydrogen from microplastics with Co_3O_4 NPs, EDX analysis is used to verify the chemical composition and purity of the catalyst, [81]. The key interpretations highlighted in this analysis are as follows:

The presence of only Cobalt (Co) and Oxygen (O) peaks in the spectrum proves that the synthesized nanoparticles are of high purity and that no impurities were formed during the preparation process, [82].

The atomic percentage ratios in the EDX results show how close the Co_3O_4 compound is to the theoretical cobalt/oxygen (Co/O) ratio (3/4). The closeness of the experimental values (e.g., 43.2% Co and 56.8% O) to this ratio confirms the successful formation of the spinel phase structure and high H_2 productions, [83].

EDX mapping analysis shows whether the Co and O elements are homogeneously distributed on the sample. The regular distribution of active canters on the surface is a critical indicator of reaction yield in photocatalytic H_2 production.

3.4 UV-vis Absorption Spectrum of Co_3O_4 NPs

Optical properties of photocatalyst play a vital role in photocatalytic processes. Therefore, it will be of great significance to determine the optical band gap of the prepared Co_3O_4 NPs. The UV-vis absorption spectrum of Co_3O_4 NPs was obtained in the applied wavelength of 200–900 nm (Fig. 10).

* Figure 10 can be found in the Appendix section.

The obtained UV-vis absorption spectrum of Co_3O_4 NPs has been illustrated in Fig. 10a. The UV-vis absorption spectrum of Co_3O_4 NPs exhibited the presence of absorption band between the wavelengths of 550–660 nm. To determine the band gap of the prepared Co_3O_4 NPs, Tauc-relation has been applied. The Tauc-plot of the Co_3O_4 NPs has been presented in inset of Fig. 10b. The observations showed that Co_3O_4 NPs has a band gap of 2.35 eV.

A band gap of 2.35 eV is a highly strategic value for photocatalytic applications and solar energy utilization. Here's the importance of this value and its place in the context of Co_3O_4 NPs. Approximately 45% of the solar spectrum is visible light. 2.35 eV corresponds to the green-yellow light region in the electromagnetic spectrum. This means that your material can efficiently absorb visible light as well, not just relying on UV light (only 5% of the sun). For an ideal photocatalyst, the band gap is generally desired to be between 1.23 eV (the theoretical lower limit for water dissociation) and 3.0 eV. 2.35 eV is both narrow enough to collect light and wide enough to maintain the redox potential of photoexcited electron/hole pairs. Co_3O_4 is generally a "p-type" semiconductor and typically exhibits two different band gap values in the literature ($E_{g1} \approx$ 1.4-1.5 eV and $E_{g2} \approx$ 2.1-2.8 eV values are reported for Co_3O_4) [84], [85]:

The 2.35 eV value we found is highly consistent with the second band gap (O 2p → Co 3d), which typically represents charge transfer transitions. If other Co_3O_4 derivatives (e.g., doped or nanostructured ones) have a wider band gap (e.g., 3.0 eV), the material will utilize visible light better than them. However, even though it absorbs less light than pure forms showing a band gap of around 1.5 eV, its oxidation potential (the strength of the holes) is likely higher. As the band gap narrows, light absorption increases, power may decrease. 2.35 eV generally provides sufficient thermodynamic driving force for the decomposition (degradation) of organic pollutants or the oxidation of water. Compared to other cobalt-based catalysts, this value provides information about the material's crystal structure, grain size, or surface defects. A lower band gap generally indicates better conductivity and photocatalytic activity.

In summary, 2.35 eV places in Co_3O_4 NPs are a visible light activated category, indicating a significant advantage over commercial TiO_2 materials (3.2 eV - UV only) for harvesting solar energy. UV-vis spectrum analysis is used to determine how efficiently the material absorbs light and its energy levels (band gap), [84], [85]. Key interpretations from these analyses are as follows:

Two main absorption bands are generally observed in the Co_3O_4 spectrum, [86], [87]. These bands originate from the different oxidation states of spinel-structured cobalt ions and their interactions with oxygen: In the visible region (~420-450 nm) the peaks represent $O^{-2} \rightarrow Co^{+3}$ charge transfer transitions. This wide absorption range indicates that Co_3O_4 can be active not only under UV but also under visible light, which constitutes a large part of the solar spectrum. The band gap of a photocatalyst for H_2 production determines its ability to provide the energy required for water decomposition, [88], [89]. Co_3O_4, as a p-type semiconductor, generally exhibits two different band gap values. Changes in the UV-vis spectrum are used to explain the reasons for the increase in H_2 production performance, [90], [91]. If Co_3O_4 is combined with another material (e.g., g-C_3N_4 or ZnO) to form a nanocomposite, the shift of the absorption edge to longer wavelengths is interpreted as an increase in photocatalytic activity. An increase in absorption intensity in the spectrum leads to the formation of more photo-generated charge carriers (electron-hole pairs), which directly supports the H_2 production rate. The slight broadening or shifting of absorption bands as the nanoparticle size decreases is explained by quantum confinement effects, indicating that the increased surface area provides a larger active site, [92].

Two different oxidation states persist in the cobalt (Co^{3+} and Co^{2+}) ion which may the reason for the existence of two absorption peaks in the UV-vis spectroscopy. The charge transfer processes from O^{2-} to Co^{2+} and O^{2-} to Co^{3+} leads to the higher band gap and lower band gap energy respectively which was responsible for the existence of absorption bands. Band gaps calculated for Co_3O_4 NPs in the literature generally range between 1.4 eV and 2.4 eV. A narrower band gap (e.g., ≈ 1.5 eV) demonstrates that the material can absorb lower-energy (longer wavelength) visible light. This increases the efficiency of solar energy utilization.

In the study performed by Vennela et al., [93], the two broad absorbance peaks were observed between 500-600 nm and 800-850 nm respectively for all the Co_3O_4 NPs, were in good agreement with the previous reports, [94]. The optical properties of the synthesized materials deliver the impurity levels, energy band structure, localized defects, excitons, lattice vibrations and certain magnetic excitations, [95]. From the plots of (αhυ)2 vs (hυ), direct band gap was found to be 1.29 eV and 3.34 eV for Co_3O_4-006, 1.39 eV and 3.53 eV for Co_3O_4-007, 1.59 eV and 3.58 eV for Co_3O_4-008 and 1.63 eV and 3.65 eV for Co_3O_4- 009 NPs. In addition, the quantum confinement effect may also be one of the reasons for linear increase in band gap energy, [96].

In the study performed by Gowthami et al., [97], the formation of Co_3O_4 NPs is indicated by a UV–visible absorption peak at 409 nm. In their research focuses on two distinct absorption bands, between 200 and 340 nm and 336 and 409 nm. According to published research, these bands can be assigned to the $O^{2\ -} \rightarrow CO^{2+}$ and $O^{2\ -} \rightarrow CO^{3+}$ charge transfer processes, respectively. In addition, an absorption peak at around 238 nm confirmed the successful formation of Co_3O_4 NPs.

In another study performed by Mohammed et al., [80], the band gap energy of 2.09 eV was revealed by the analysis, suggesting that Co_3O_4 NPs are appropriate photocatalysts under the visible light. In the study performed by Kaur et al., [98], a particular absorption at two separate wavelengths in the 200–650 nm range, focused at 267 nm and 524 nm, respectively, revealing the phenolic chemicals present that are in charge of the green production of Co_3O_4 NPs. The existence of the first band close to the UV dimension, which is due to the $O^{2-} \rightarrow Co^{2+}$ charge transfer process, and the second absorption band close to the green region, which is assigned to the $O^{2-} \rightarrow Co^{3+}$ charge transfer, indicates that Co_3O_4 NPs have formed. They observed two distinct absorption peaks at different frequencies as a result of the ligand-to-metal charge transfer method, such as the $O^{2-} \rightarrow Co^{2+}$ charge transfer transition for the first absorption band at 267 nm and the $O^{2-} \rightarrow Co^{3+}$ charge transfer transition for the second absorption band at 524 nm, respectively.

3.5 FTIR Analysis Results

FTIR graphs of Co_3O_4 NPs are based primarily on two characteristic sharp peaks belonging to the metal-oxygen bonds in the spinel structure. These graphs are used to verify the formation of Co_3O_4 and its interaction with other components (graphene, carbon nanotubes, polymers, etc.) within the nanocomposite. The main FTIR spectrum values are 1145 cm^{-1}, 1397 cm^{-1}, 1645 cm^{-1} and 3500 cm^{-1} for C=O, O-H, C=O and O-H bonds, respectively (Fig. 11).

* Figure 11 can be found in the Appendix section.

Characteristic FTIR peaks were the main bands observed in the graph for pure Co_3O_4 nanostructures are, [99]:

(a) Metal-oxygen bonds (Co-O) have a (a1) ≈ 580 cm^{-1} corresponds to the vibrational mode of Co^{+3} ions in octahedral regions, [100]. (a2) has ≈ 668 cm^{-1} and is related to the vibrational mode of Co^{+2} ions in tetrahedral regions. In some studies, these values may shift slightly depending on the synthesis method for 552 and 657 cm^{-1} planes.

(b) Surface groups have (b1) ≈ 3440 cm^{-1} with a broad band showing the stretching vibration of water molecules or hydroxyl (-OH) groups adsorbed on the surface, [101]. (b2) have ≈ 1630 cm^{-1} and represents the bending vibration of water molecules.

Other peaks observed in nanocomposites when Co_3O_4 is combined with a matrix and additional bands depending on the type of composite: (a) Graphene/rGO composite peaks belonging to carbon groups such as C=C (1622 cm^{-1}) and C-O-C (1045 cm^{-1}) are seen together with Co-O peaks. (b) Polymer composites like PPy vibrations belonging to functional groups in the polymer chain accompany metal oxide peaks. (c) Silica-coated structures (Co_3O_4@SiO_2) have strong asymmetric stretching bands of Si-O-Si bonds may become dominant, [102], [103].

Residues from precursor materials used during synthesis may also leave traces. For example, if cobalt nitrate was used, peaks of nitrate (NO_3^{-1}) ions around 1398 cm^{-1} may be observed.

3.6 HRTEM Analysis Results

HRTEM graphs for Co_3O_4 NPs are used to visualize the crystal structure, atomic arrangement, and interface interactions between components of these materials at the atomic scale. HRTEM images of Co_3O_4 NPs were shown for 500 nm (Fig. 12a) and 100 nm (Fig. 12b) image size, respectively.

* Figure 12 can be found in the Appendix section.

HRTEM analyses typically reveal the following structural details in Co_3O_4 NPs, [104]: (a) Crystal lattice lines (Lattice fringes) were clear lines representing the distance between atomic planes. For example, interplane distance (d-spacing) values for specific crystal planes such as (311), (220), or (111) for Co_3O_4 can be calculated from these lines. (b) In the composite structures (e.g., Co_3O_4/Graphene or Co_3O_4/Carbon Nanotube, CNT), interfaces phases be clearly distinguished with HRTEM. This confirms epitaxial growth or chemical bonding between phases. (c) Morphology and size in specific geometric forms of nanoparticles, such as cubes, rods, or plates, and their typical sizes in the 10-50 nm range are visualized in these graphs.

In the common Co_3O_4-based nanocomposites studied with HRTEM in the literature include, [105], [106]: (a) Co_3O_4/rGO (Reduced graphene oxide) used to enhance the electron transfer in supercapacitor and battery applications. Co_3O_4 nanocrystals dispersed on graphene layers are clearly observed in HRTEM images. (b) IN Co_3O_4/CNT nanocomposites Co_3O_4 NPs attached to the outer walls of nanotubes and this provides high surface area and conductivity. (c) In Co_3O_4/Polymer nanocomposites has some hole transport layer in photovoltaic cells. Atomic-scale images help analyse the interaction between polymer chains and the oxide surface.

3.7 H_2(g) Generation in 100 mg/l PA (Nylon), PAK, PMMA, PE and AC MPs Concentrations at increasing Co_3O_4 NPs concentrations

The photocatalytic properties of the increasing Co_3O_4 NPs concentrations on H_2 productions were investigated in presence of 100 mg/l Polyamide (PA, Nylon) Polyacrylate (PAK) and Polymethyl methacrylate (PMMA), Polyethylene (PE) and Acrylates Copolymers (AC).

The effects of increasing concentrations of Co_3O_4 NPs (1, 2, 3 and 4 mg/l) on H_2 productions of microplastics is illustrated in Fig. 13. It was observed that the maximal H_2 productions were detected as 180 mmol/g Co_3O_4 NP.h, 108 mmol/g Co_3O_4 NP.h and 105 mmol/g Co_3O_4 NP.h, at 100 mg/l PE, PAK and PA (Nylon) microplastic concentrations, respectively, after 25 min (0.40 h) retention time at 2 mg/l Co_3O_4 NPs concentrations (Fig. 13a, b, c).

The maximal H_2 productions were found to be slightly low in PMMA (82 mmol/g Co_3O_4 NP.h and AC (87 mmol/g Co_3O_4 NP.h) containing samples after 25 min (0.4 h) retention time at 2 mg/l Co_3O_4 NPs concentration (Fig. 13d and e).

* Figure 13 can be found in the Appendix section.

This clearly suggested that Co_3O_4 NPs exhibited excellent photocatalytic properties for the generation of H_2 in presence of PE, PAK and PA MPs as scavenger agents. The amount of photocatalyst may also significantly affect the photocatalytic H_2 generation. It is important to optimize the amount of photocatalyst for the generation of H_2. H_2 production from polymers varies greatly depending on the type of polymer (PE, PP, PET, PLA) and the catalyst system, [68,107]. PET and PLA are biodegradable/hydrolysable microplastics and exhibited highest H_2 efficiency because they are structurally more susceptible to oxidation. For example, H_2 production was found to be 503.9 mmol/g nanocomposite. h for 200 mg/l PLA in optimized Z-scheme systems, [108]. Since the polyolefins (PP) C-C bonds are more difficult to break, production rates are generally low, [109]. The H_2 total yields was measured as 379 mmol/g polymer h in heterojunction systems like conjugated polymer namely dibenzothiophene-S,S-dioxide-*alt*-benzodithiophene

(DBTSO-BDTO) and cadmium sulfide (CdS) for photocatalytic H_2 production, [110].

The efficiency of photocatalytic H_2 production by polymers is directly dependent on how fundamental mechanisms such as light harvesting, charge separation rate, and surface reaction dynamics interact with the molecular and structural architecture of the polymer, [107], [108], [109]. Co_3O_4 increases charge separation when added to semiconductors such as g-C_3N_4 or ZnO. For example, loading 20% Co_3O_4 onto ZnO increases the H_2 production rate by 11.8 times compared to pure ZnO, reaching 793.2 μmol/g.h, [110]. Co_3O_4@g-C_3N_4 heterojunctions provide approximately 35-40% higher yields (e.g., 67.17 μmol/g.h) in polymer reformation compared to pure components, [110]. Co_3O_4-based systems are versatile catalysts that can achieve "impressive" rates of 21.128 ml/min.g in H_2 production from carriers such as $NaBH_4$, not only in polymer, [110].

The sequential arrangement of electron-rich (donor) and electron-poor (acceptor) units in the polymer chain is one of the most critical strategies determining the photocatalytic efficiency, [111], [112]. The D-A structure of nanocomposite also creates a permanent dipole moment and a local electric field within the polymer. This field causes light-excited electrons and holes to move rapidly away from each other, reducing the recombination rate. Conjugated porous structures and porous polymer structures with covalent organic frameworks increase the H_2 efficiency through surface area and bulk conductivity, [113], [114], [115]. High surface area of porous structures offers more active sites for water molecules. Defined pore sizes accelerate the reaction kinetics of H_2 production by facilitating both the entry of water and the rapid removal of H_2 gas produced from the structure. Not only the main chain of the polymer, but also the side chains attached to it affect the mechanism, [116], [117], [118]. The addition of hydrophilic side chains to a hydrophobic main chain allows water to penetrate better into the polymer surface and interior. This reduces proton transfer resistance at the polymer-water interface. High local dielectric constants break the strong exciton binding energy in organic polymers, facilitating the release of electrons.

Poojitha et al., [119], found a giant H_2 evolution efficacy (3012 μmol/g.h) in 300 min by using 100 g/l CdS:(Ce, Ga) which is 13.9 times larger than that of the bar CdS sample under simulated solar illumination, with lactic acid employed as a scavenger agent in the reaction medium. The heightened H_2 production efficiency of the nanocomposites sample could be attributed to several factors. Primarily, the emergence of abundant charge carriers due to the co-doping process plays a crucial role. Additionally, the presence of defective sites and trap locations contributes to this enhancement. Ultimately, the reduction in the recombination rate between charge carriers serves as a fundamental mechanism driving the effective photocatalytic H_2 production observed sample, [120], [121]. The g-C_3N_4/MoO_3-x composite exhibits a notably enhanced photocatalytic H_2 production efficiency and excellent cycling stability when compared to sonicated g-C_3N_4 nanosheets. The g-C_3N_4/MoO_3-x composite with a mass percent of 27.50% achieves the highest H_2 generation activity of 209.2 μmol/h under solar light and an apparent quantum efficiency of 4.40% when irradiated at 365 nm, which is 2.63 times greater than g-C_3N_4.

Chen et al., [122], developed a novel Z-scheme 2D-0D $MnPS_3$-$Cs_4W_{11}O_{35}$ composite for photocatalytic H_2 evolution. The $MnPS_3$-$Cs_4W_{11}O_{35}$ composites achieve the highest H_2 evolution rate of 99.6 μmol/g.h when the $Cs_4W_{11}O_{35}$ content is 10.9% by mass, which is 2.9 times greater than that of $MnPS_3$ nanosheets alone.Moreover, the photocatalytic performance of $MnPS_3$-$Cs_4W_{11}O_{35}$ remains almost stable afterfour cycles. $MnPS_3$ is a non-toxic p-type direct bandgap semiconductor known for its strong visible light absorption capabilities. This unique structure makes MnPS3 a promising candidate for photocatalysts, as it possesses a suitable bandgap and favorable band positions for photocatalytic water splitting. Despite these advantages, the photocatalytic H_2 evolution rate of $MnPS_3$ nanosheets remains relatively low (21.2 mmol/g.h) due to a high photoelectron–hole recombination rate and insufficient oxygen production.

Kaykhaii et al., [123], found that 60 particles/l of micrometer-sized polyethylene terephthalate reduces hydrogen production by 30%, while 200 particles of it yields 63.6% more hydrogen.

The reasons of slightly lower H_2 productions in PMMA and AC microplastics cannot be explained only by higher molecular weights but also by structural and chemical dynamics as follows:

PMMA and AC structurally have "quaternary carbon" atoms. When these polymers are exposed to energy (photolysis or radiolysis), the free radicals become trapped on the polymer chain. The side groups (methyl and ester groups) of PMMA surround the radicals on the main chain, making it difficult for them to recombine or interact with water molecules and detach H_2. This "steric hindrance" slows down the rate of reactions leading to H_2 formation.

Although, PMMA and AC polymers possess high optical transparency, they can exhibit "self-shielding" at certain wavelengths (particularly in the UV region). The high reflectivity index of the polymer surface prevents photons needed by the photocatalyst from reaching the depth. Light is scattered within the dense amorphous structure of the polymer; this reduces the efficiency of energy delivery to the active canters (e.g., a catalyst embedded in the polymer).

H_2 production is generally a surface phenomenon. The high molecular weight of PMMA and AC causes the polymer chains to be very tightly packed. The small H_2 bubbles are trapped within the polymer matrix. Because the diffusion coefficient is low, H_2 cannot quickly escape from the system, which can force the chemical equilibrium to reverse. The aforementioned polymers are generally hydrophobic. Access of water molecules to the polymer surface or to the active sites within it is restricted. The low contact with water reduces the yield because it reduces access to the direct proton source. Acrylates, such as PMMA, tend to expend energy on chain vibrations (heat) or side group elimination (e.g., $COOCH_3$ cleavage) rather than breaking H_2 bonds. That is, the absorbed energy is directed to the polymer's degradation channels instead of the "useful" chemical work of H-H bond formation.

The low H_2 production in the aforementioned microplastics, stems from energy trapping at the surface, difficulty in transporting water to the active sites, and the polymer structure stabilizing radicals to terminate the process.

PET after photolysis in NaOH (PET + NaOH +UV) was identical to that of the untreated PET. The spectrum after photolysis in water (PET+H_2O+UV) shows weak bands at 2997 and 2945 cm^{-1}, corresponding to the asymmetric and symmetric stretching C-H vibrations of the CH_2 groups. The strong bands at 1762 and 1217-1098 cm^{-1} correspond to C=O and C-O stretching vibrations, respectively, [124], [125]. The weak band at 1456 cm^{-1} could be assigned to the deformation vibration of the O-H group, [124], [125].

Han et al., [126], found that the g-C_3N_4/CoO/CoP catalyst exhibits a hydrogen evolution activity of 1277.9 µmol/g·h, which is 4 times higher than that of g-C_3N_4/CoO (with g-C_3N_4/alone showing no H_2 evolution activity under optimized conditions,). Its performance is comparable to that of the commonly used Pt cocatalyst. Lin et al., [127], investigated the H2 production from ultra-high molecular weight polyethylene (UHMWPE) by using FeSA-hCN nanocomposite. The performance improvement may be attributed to the tight bonding of N-P bonds, which effectively promotes the transport of photogenerated carriers, while the increased loading of CoP provides more active sites in FeSA-hCN nanocomposite and it's band structure. The mixture of FeSA-hCN and plastic degradation products further achieves a H_2 evolution of 42 µmol/h under illumination. The formation of hydrogen radicals from the photoreaction products of PET and PLA could be explained by the breaking of C-H and /or O-H groups, [128]. In the NaOH suspensions, R-COOH is neutralised into R-COO$^-$, and the reaction cannot occur. Moreover, in these alkaline suspensions, the hydrogen radicals can react with hydroxide ions, [129], which also explains the decrease of hydrogen yields.

Ren et al, [130], investigated the polyethylene terephthalate microplastics (PET MPs) on the semi-continuous H_2 production under mesophilic and thermophilic fermentation were investigated. Results indicated that PET MPs can enhance the semi-continuous H_2 production performance, and the highest H_2 production rates in mesophilic and thermophilic MPs supplemented groups were 4.85 and 3.6 l/l.d, which were 21.60% and 63.60% higher than the control groups, respectively. During the stable operation period, H_2 production rate and H_2 content in the mesophilic PET MPs supplemented group were higher than those obtained from the thermophilic condition, [131], [132], [133], [134]. PET MPs could serve as immobilization carriers and favour, the growth of H_2-producing bacteria under mesophilic and thermophilic fermentation, thereby enhancing the semi-continuous H_2 production performance, [135], [136], [137], [138].

3.8 Effect of increasing time on $H_2(g)$ Generation in 100 mg/l PA (Nylon), PAK, PMMA, PE and AC MPs Concentrations at 2 mg/l Co_3O_4 NPs concentrations

In order to detect the effects of increasing photocatalytic degradation times (10, 15, 20, 25, 30, 35, 40, and 45 min- or 0.17, 0.25, 0.33, 0.42, 0.50, 0.58, 0.67 and 0.75 h) on H_2 production of 100 mg/l PA, PAK, PE, PMMA, and AC MPs, the studies were performed at 2 mg./l Co_3O_4 NPs concentrations (Fig. 14).

* Figure 14 can be found in the Appendix section.

The data aforementioned above showed that Co_3O_4 NPs is excellent photocatalyst for photocatalytic H_2 generation reactions from micropollutants namely PA (Nylon), PAK, PE, PMMA, and AC MPs, respectively, at 2 mg/l Co_3O_4 NPs at increasing photocatalytic degradation times (10, 15, 20, 25, 30, 35, 40, and 45 min). The maximum H2 production yields for all studied microplastics were detected after 0.42 h (25 min).

3.9 Reusability of Co_3O_4 NPs

It is very important to examine the stability or reusability of the Co_3O_4 NPs. Therefore, the reusability of the prepared Co_3O_4 NPs was investigated during 65 cycles. The results were given in Fig. 15.

* Figure 15 can be found in the Appendix section.

It can be seen that Co_3O_4 NPs exhibited excellent reusability after 65 cycles and can be reused for further H_2 generation processes. After, 65 cases 99 mmol/g H_2 production was detected.

4 Conclusions

In the present study, Co_3O_4 NCs were synthesized and employed as photocatalysts for hydrogen production under solar simulated conditions from microplastics namely Polyamide (PA, Nylon), Polyacrylate (PAR), Polyethylene (PE), Polymethyl methacrylate (PMMA) and Acrylates Copolymer (AC).

The XRD analysis of the Co_3O_4 NPs showed the purity and the crystallinity properties of the photocatalyst while SEM data have shown that Co_3O_4 NPs contain some agglomerated clustered particles.

EDX spectrum of Co_3O_4 NPs exhibited the presence of Co and O.

The average particle size of Co_3O_4 NPs was less than 15 nm. In our study, the surface area of Co_3O_4 NPs were measured as 82 m^2/g, indicating more contact points in large surface with ligth and microplastics resulting in more H_2 production.

The main FTIR spectrum values are 1145 cm^{-1}, 1397 cm^{-1}, 1645 cm^{-1} and 3500 cm^{-1} for C=O, O-H, C=O and O-H bonds, respectively.Specific geometric forms of Co_3O_4 NPs, such as cubes, rods, or plates, and their typical sizes in the range of 10-40 nm range are visualized in HRTEM graphs

With a band gap energy of 2.35 eV in Co_3O_4 NPs, sufficient thermodynamic driving force for the decomposition (degradation) of organic pollutants and for the oxidation of water was supplied. Compared to other cobalt-based catalysts, this band gap energy provides information about the material's crystal structure, grain size, and surface defects. A lower band gap generally indicates better conductivity and photocatalytic activity at UV-vis absorption spectrum.

The maximal H_2 productions were detected as 180 mmol/g Co_3O_4 NP.h, for PE; 108 mmol/g Co_3O_4 NP.h for PAK and 105 mmol/g Co_3O_4 NP.h, for PA at 100 mg/l PE, PAK and PA microplastic concentrations, respectively, after 0.40 h retention time at 2 mg/l Co_3O_4 NPs concentrations. The maximal H_2 productions were found to be slightly low in PMMA (82 mmol/g Co_3O_4 NP.h and AC (87 mmol/g Co_3O_4 NP.h) after 0.4 h at 2 mg/l Co_3O_4 NPs at initial 100 mg/l PMMA and AC microplastic concentrations.

For maximum microplastic yields the optimal operations conditions were 2 mg/l Co_3O_4 NPs concentration, 0.4 h and 100 mg/l initial microplastic (PA, PAR, PE, PMMA and AC) concentrations.

The reusability studies showed that the nanocomposites exhibited the same H_2 productions for 64 cycles. Co_3O_4 NPs possessed slightly improved photocatalytic degradation of microplastics studied in this work.

Acknowledgement:
Experimental analyzes in this study were performed at the Laboratories of the Canada Research Center, Ottawa, Canada. The authors would like to thank this body for providing financial support.

The List of Abbreviations

$H_2(g)$: Hydrogen gas
MPs: Microplastics
Co_3O_4: Cobalt oxide
NCs: Nanocomposites
XRD: X-Ray Diffraction Analysis
SEM: Scanning Electron Microscope Analysis
EDX Energy Dispersive X-Ray Analysis
HRTEM: High Resolution Transmission Electron Microscopy Analysis
FTIR: Fourier Transform Infrared Spectroscopy Analysis
(PA, Nylon): Polyamide (PA, Nylon),
PAK: Polyacrylate,
PE: Polyethylene,
PMMA: Polymethyl methacrylate
AC: Acrylates Copolymer
PPCPs: Pharmaceuticals and personal care products
R-COOH: Carboxylic acid
$R-NH_2$: Amines group
OH: Hydroxyl
LDPE MPs: Low density PE MPs
HDPE MPs: High density PE MPs
MDPE MPs: Medium-density PE MPs
PEX or XLPE MPs: Cross-linked polyethylene PE MPs
PAHs: Polyaromatic Hydrocarbons
$O_2(g)$: oxygen gas
$CO_2(g)$: carbon dioxide
LLDPE MPs: Linear low-density polyethylene PE MPs
CH_4: Methane
C_2H_4: Ethylene
$(-CH_2-)$: Methylene groups
PSAs: Pressure-sensitive adhesives

UHMWPE MPs: Ultra-high-molecular-weight PE MPs
ULMWPE MPs or PE-WAX MPs: Ultra-low-molecular-weight PE MPs
HMWPE MPs: High-molecular-weight PE MPs
HDPE MPs: High-density PE MPs
HDXLPE MPs: High-density cross-linked PE MPs
PEX MPs or XLPE MPs: Cross-linked PE MPs,
MDPE MPs: Medium-density PE MPs
LLDPE MPs: Linear low-density PE MPs
LDPE MPs: Low-density PE MPs,
VLDPE MPs: Very-low-density PE MPs
CPE MPs: Chlorinated PE MPs
PMMA MPs: Polymethyl methacrylate MPs
CO: Carbon monoxide
UV: Ultraviolet light
R-groups: Radical groups
ACM: Acrylic acid ester and 2-chloroethyl vinyl ether copolymer)
ANM: Acrylic acid ester and acrylonitrile copolymer).
SAP: Super Absorbent Polymer
VOCs: Volatile organic compounds
TMPTA: Trimethylolpropane triacrylate
PEM: Polymer Electrolyte Membrane

References:

[1] K. E. Murray, S. M. Thomas, A. A. Bodour, Prioritizing Research for Trace Pollutants and Emerging Contaminants in the Freshwater Environment, *Environment and Pollution,* Vol.158, 2010, pp. 3462–3471.

[2] P. E. Rosenfeld, L. G. Feng, *Emerging Contaminants*, In Risks of Hazardous Wastes; Elsevier: Amsterdam, The Netherlands, pp. 215–222, 2011.

[3] T. Rasheed, M. Bilal, F. Nabeel, M. Adeel, H. M. Iqbal, Environmentally-Related Contaminants of High Concern: Potential Sources and Analytical Modalities for Detection, Quantification, and Treatment, *Environment International,* Vol.122, 2019, pp. 52-66.

[4] C. G. Daughton, Non-Regulated Water Contaminants: Emerging Research, *Environmental Impact Assessment Review*, Vol.24, 2004, pp. 711–732.

[5] OECD (Organisation for Economic Cooperation and Development). 2010. *Short Guidance on the Threshold Approach for Acute Fish Toxicity*, Series on Testing and Assessment no. 126. ENV/JM/MONO(2010)17. Paris:OECD. Available: http://iccvam.niehs.nih.gov/SuppDocs/FedDocs/OECD/OECDGD126.pdf [accessed 20 March 2026]. (2010).

[6] US EPA, "*Origins and Fate of PPCPs in the Environment*" (PDF). Pharmaceuticals and Personal Care Products. EPA, National Exposure Research Laboratory, (March 2006).

[7] WHO (World Health Organization). 2011. *Pharmaceuticals in Drinking Water*, WHO/HSE/WSH/11.05. Geneva:WHO. Available: http://www.who.int/water_sanitation_health/publications/2011/pharmaceuticals_20110601.pdf [accessed 18 March 2026], 2011.

[8] B. W. Brooks, T. M. Riley, R. D. Taylor, Water Quality of Effluent Dominated Stream Ecosystems: Ecotoxicological, Hydrological, and Management Considerations, *Hydrobiologia,* Vol.556, 2006, pp. 365–379.

[9] J. Corcoran, C. J. Winter, C. R. Tyler, Pharmaceuticals in the Aquatic Environment: A Critical Review of the Evidence for Health Effects in Fish, *Critical Reviews in Toxicology,* Vol.40, 2010, pp. 287–304.

[10] J. Gomes, R. Costa, R. M. Quinta-Ferreira, R. C. Martins, Application of Ozonation for Pharmaceuticals and Personal Care Products Removal from Water, *Science of the Total Environment,* Vol.586, 2017, pp. 265–283.

[11] D. J. Lapworth, N. Baran, M. E. Stuart, R. S. Ward, Emerging Organic Contaminants in Groundwater: A Review of Sources, Fate and Occurrence, *Environment and Pollution*, Vol.163, 2012, pp. 287-303.

[12] S. Zhang, S. Gitungo, L. Axe, J. E. Dyksen, R. F. Raczko, A Pilot Plant Study Using Conventional and Advanced Water Treatment Processes: Evaluating Removal Efficiency of Indicator Compounds Representative of Pharmaceuticals and Personal Care Products, *Water Research,* Vol.105, 2016, pp. 85–96.

[13] X. Yuan, J. Hu, S. Li, M. Yu, Occurrence, Fate, and Mass Balance of Selected Pharmaceutical and Personal Care Products (PPCPs) in an Urbanized River, *Environment and Pollution,* Vol.266, 2020, 115340.

[14] D. W. Brew, M. C. Black, M. Santos, J. Rodgers, W. M. Henderson, Metabolomic Investigations of the Temporal Effects of Exposure to Pharmaceuticals and Personal Care Products and their Mixture in the Eastern Oyster (Crassostrea virginica), *Environmental Toxicology and Chemistry*, Vol.39, 2020, pp. 419–436.

[15] M. Ortúzar, M. Esterhuizen, D. R. Olicón-Hernández, J. González-López, E. Aranda, Pharmaceutical Pollution in Aquatic

Environments: A Concise Review of Environmental Impacts and Bioremediation Systems, *Frontiers in Microbiology,* Vol.13, 2022, 869332.

[16] T. A. Ternes, A. Joss, H. Siegrist, Peer Reviewed: Scrutinizing Pharmaceuticals and Personal Care Products in Wastewater Treatment, *Environmental Science & Technology,* Vol.38, 2004, pp. 392A–399A.

[17] J. P. Meador, A. Yeh, E. P. Gallagher, Determining Potential Adverse Effects in Marine Fish Exposed to Pharmaceuticals and Personal Care Products with the Fish Plasma Model and Whole-Body Tissue Concentrations, *Environment and Pollution,* Vol.230, 2017, pp. 1018–1029.

[18] Y. Yang, Y. S. Ok, K.-H. Kim, E. E. Kwon, Y. F. Tsang, Occurrences and Removal of Pharmaceuticals and Personal Care Products (PPCPs) in Drinking Water and Water/Sewage Treatment Plants: A Review, *Science of the Total Environment,* Vol.596–597, 2017, pp. 303–320.

[19] D. Barraclough, T. Kearney, A. Croxford, Bound Residues: Environmental Solution or Future Problem?, *Environment and Pollution*, Vol.133, 2005, pp. 85–90.

[20] R. Kreuzig, S. Höltge, Investigations on the Fate of Sulfadiazine in Manured Soil: Laboratory Experiments and Test Plot Studies, *Environmental Toxicology and Chemistry,* Vol.24, 2005, pp. 771–776.

[21] J. Wang, S. Wang, Removal of Pharmaceuticals and Personal Care Products (PPCPs) from Wastewater: A Review, *Journal of Environmental Management,* Vol.182, 2016, pp. 620–640.

[22] Y. Huang, C. Wong, J. Zheng, H. Bouwman, R. Barra, B. Wahlström, L. Neretin, M. Wong, Bisphenol A (BPA) in China: A Review of Sources, Environmental Levels, and Potential Human Health Impacts, *Environment International,* Vol.42, 2012, pp. 91–99.

[23] I. Tamura, Y. Yasuda, K.-I. Kagota, S. Yoneda, N. Nakada, V. Kumar, Y. Kameda, K. Kimura, N. Tatarazako, H. Yamamoto, Contribution of Pharmaceuticals and Personal Care Products (PPCPs) to whole Toxicity of Water Samples Collected in Effluent Dominated Urban Streams, *Ecotoxicology and Environmental Safety*, Vol.144, 2017, pp. 338–350.

[24] Q. Wang, M. Nakabayashi, T. Hisatomi, S. Sun, S. Akiyama, Z. Wang, Z. Pan, X. Xiao, T. Watanabe, T. Yamada, N. Shibata, T. Takata, K. Domen, Oxysulfide Photocatalyst for Visible-Light-Driven Overall Water Splitting, *Nature Materials,* Vol.18, 2019, pp. 827–832.

[25] E. E. Magat, B. F. Faris, J. E. Reith, L. F. Salisbury, Acid-catalyzed Reactions of Nitriles. I. The Reaction of Nitriles with Formaldehyde1, *Journal of the American Chemical Society,* Vol.73, No.3, 1951, pp. 1028–1031.

[26] M. M. Lakouraj, M. Mokhtary, Synthesis of Polyamides from p-Xylylene Glycol and Dinitriles, *Journal of Polymer Research,* Vol.16, No.6, 2009, 681.

[27] E. Penzel, *Polyacrylates. Ullmann's Encyclopedia of Industrial Chemistry*, Weinheim: Wiley-VCH. pp. a21_157, ISBN 978-3-527-30673-2, 2000.

[28] "*Acrylic Elastomer Composition (Patent 6015860)*", PatentStorm. Archived from the original on 2011-06-12, Retrieved 2026-03-23.

[29] Plastics Design Library, *Handbook of Plastics Joining: A Practical Guide*, Norwich, New York: Plastics Design Library. p. 326. ISBN:1-884207-17-0, 1997.

[30] K. S. Whiteley, T. G. Heggs, H. Koch, R. L. Mawer, W. Immel, *Polyolefins,* Ullmann's Encyclopedia of Industrial Chemistry, ISBN:3-527-30673-0, 2000.

[31] W. Kaiser, Kunststoffchemie für Ingenieure von der Synthese bis Zur Anwendung (3. ed.). München: Hanser, Germany, ISBN:978-3-446-43047-1, 2011.

[32] C. I. Chung, *Extrusion of Polymers: Theory and Practice*, 2nd ed. Hanser: Munich, Germany, 2010.

[33] V. Ostrovskii, V. A. Khodzhemirov, S. P. Kostareva, Ethylene Polymerization Heat (abstract) in Doklady, *Chemistry,* Vol.184, No.1, 1969, pp. 103–104.

[34] E. Prideaux, (3 November 2007), *Plastic Incineration Rise Draws Ire*, The Japan Times, Archived from the original on 22 November 2012. Retrieved 20 March 2026, 2007.

[35] V. Tournier, S. Duquesne, F. Guillamot, H. Cramail, D. Taton, A. Marty, I. André, Enzymes' Power for Plastics Degradation, *Chemical Reviews,* Vol.123, No.9, 2023, pp. 5612–5701.

[36] S.-J. Royer, S. Ferrón, S. T. Wilson, D. M. Karl, Production of Methane and Ethylene from Plastic in the Environment, *Plos One*, Vol.13, No.8, 2008, e0200574.

[37] W. R. Zeng, S. F. Li, W. K. Chow, Preliminary Studies on Burning Behaviour of Polymethylmethacrylate (PMMA), *Journal of Fire Sciences,* Vol.20, No.4, 2002, pp. 297–317.

[38] L. W. McKeen, The Effect of UV *Light and Weather on Plastics and Elastomers*, (4th ed.),

Washington, WA: Elsevier, p. 254. ISBN:978-0-1281-6457-0, 2019.

[39] C. Ishiyama, Y. Yamamoto, Y. Higo, Effects of Humidity History on the Tensile Deformation Behaviour of Poly(methyl–methacrylate) (PMMA) Films, *Springer Nature MRS Online Proceedings Library*, Vol.875, 2005, article number: 127.

[40] F. Cappitelli, P. Principi, C. Sorlini, Biodeterioration of Modern Materials in Contemporary Collections: Can Biotechnology Help?. *Trends in Biotechnology,* Vol.24, No.8, 2006, pp. 350–254.

[41] A. López, A. Hoess, T. Thersleff, M. Ott, H. Engqvist, C. Persson, Low-Modulus PMMA Bone Cement Modified with Castor Oil, *Bio-Medical Materials and Engineering,* Vol.21, No.5–6, 2011, pp. 323–332.

[42] B. Coxworth, B. (2025-03-03), *Simple Technique may Allow for Almost Complete Recycling of Plexiglass*, New Atlas, Retrieved 2026-03-05.

[43] T. J. Kaufmann, M. E. Jensen, G. Ford, L. L. Gill, W. F. Marx, D. F. Kallmes, Cardiovascular Effects of Polymethylmethacrylate Use in Percutaneous Vertebroplasty, *American Journal of Neuroradiology,* Vol.23, No.4, 2002, pp. 601–604.

[44] O. Takashi, S. Takahisa, S. Noboru, P. Günter, S. Helmut, W. Otto, M. Klaus, G. Helmut, *Acrylic Acid and Derivatives*, Ullmann's Encyclopedia of Industrial Chemistry. Weinheim: Wiley-VCH, Germany, ISBN:3527306730, 2003.

[45] H. J. Arpe, *Industrielle organische Chemie: bedeutende Vor- und Zwischenprodukte* (6 ed.). Weinheim: Wiley-VCH, Germany, ISBN 978-3-527-31540-6, 2007.

[46] T. Ohara, T. Sato, N. Shimizu, G. Prescher, H. Schwind, O. Weiberg, K. Marten, *Acrylic Acid and Derivatives*, Ullmann's Encyclopedia of Industrial Chemistry. Weinheim: Wiley-VCH, Germany, ISBN:978-3-527-30673-2, 2002.

[47] O. Grimaldos, F. N. Sordello, M. Passananti, P. Vernoux, From Plastic-Waste to H_2: Electrolysis of a Poly(methyl methacrylate) Model Molecule on Polymer Electrolyte Membrane Reactors, *Journal of Power Sources*, Vol.480, 2020, 228800.

[48] R. Shi, K.-S. Liu, F. Liu, X. Yang, C.-C. Hou, Y. Chen, Electrocatalytic Reforming of Waste Plastics into High Value-Added Chemicals and Hydrogen Fuel, *Chemical Communications,* Vol.57, 2021, pp. 12595-12598.

[49] E. M. N. Thiloka Edirisooriya, P. S. Senanayake, H. B. Wang, M. R. Talipov, P. Xu, H. Wang, Photo-Reforming and Degradation of Waste Plastics under UV and Visible Light for H_2 Production Using Nanocomposite Photocatalysts Acrylamide, *Journal of Environmental Chemical Engineering,* Vol.11, No.2, 2023, 109580.

[50] N. Grimaldos-Osorio, F. Sordello, M. Passananti, J. González-Cobos, A. P. Bonhommé, Vernoux, A. Caravaca, From Plastic-Waste to H_2: A First Approach to the Electrochemical Reforming of Dissolved Poly(methyl methacrylate) Particles. *International Journal of Hydrogen Energy*, Vol.48, No.32, 2023, pp. 11899-11913.

[51] S. Sekar, V. Preethi, S. Saravanan, D. Y. Kim, S. Lee, Excellent Photocatalytic Performances of Co_3O_4–AC Nanocomposites for H_2 Production via Wastewater Splitting, *Chemosphere*, Vol.286, Part.2, 2022, 131823.

[52] Z. Wang, Y. Inoue, T. Hisatomi, R. Ishikawa, Q. Wang, T. Takata, S. Chen, N. Shibata, Y. Ikuhara, K. Domen, Overall Water Splitting by Ta_3N_5 Nanorod Single Crystals Grown on the Edges of $KTaO_3$ Particles, *Nature Catalysis,* Vol.1, 2018, pp. 756–763.

[53] T. Hisatomi, K. Domen, Reaction Systems for Solar Hydrogen Production via Water Splitting with Particulate Semiconductor, *Nature Catalysis*, Vol.2, 2019, pp. 387–399.

[54] J. Jia, L. C. Seitz, J. D. Benck, Y. Huo, Y. Chen, J. W. D. Ng, T. Bilir, J. S. Harris, T. F. Jaramillo, Solar Water Splitting by Photovoltaic-Electrolysis with a Solar-to-Hydrogen Efficiency Over 30%, *Nature Communications,* Vol.7, 2016, 13237.

[55] J. H. Kim, D. Hansora, P. Sharma, J.-W. Jang, J. Lee, Toward Practical Solar Hydrogen Production – An Artificial Photosynthetic Leaf-to-Farm Challenge, *Chemical Society Reviews,* Vol.48, 2019, pp. 1908–1971.

[56] Y. Wang, T. Yin, B. C. Kelly, K. Y.-H. Gin, Bioaccumulation Behaviour of Pharmaceuticals and Personal Care Products in a Constructed Wetland, *Chemosphere*, Vol.222, 2019, pp. 275–285.

[57] H. Lyu, T. Hisatomi, Y. Goto, M. Yoshida, T. Higashi, M. Katayama, T. Takata, T. Minegishi, H. Nishiyama, T. Yamada, Y. Sakata, K. Asakura, K. Domen, An Al-Doped $SrTiO_3$ Photocatalyst Maintaining Sunlight-Driven Overall Water Splitting Activity Over 1000 h of Constant Illumination, *Chemical Science,* Vol.10, 2019, pp. 3196–3201.

[58] T. Yamada, K. Domen, Development of Sunlight Driven Water Splitting Devices Towards Future Artificial Photosynthetic Industry, *ChemEngineering,* Vol.2, No.3, 2018, 36.

[59] K. Maeda, K. Teramura, D. Lu, T. Takata, N. Saito, Y. Inoue, K. Domen, Characterization of Rh-Cr Mixed-Oxide nanoparticles Dispersed on (Ga1-xZnx)(N1-xOx) as a Cocatalyst for Visible-Light-Driven Overall Water Splitting, *The Journal of Physical Chemistry B,* Vol.110, 2006, pp. 13753–13758.

[60] Y. Goto, T. Hisatomi, Q. Wang, T. Higashi, K. Ishikiriyama, T. Maeda, Y. Sakata, S. Okunaka, H. Tokudome, M. Katayama, S. Akiyama, H. Nishiyama, Y. Inoue, T. Takewaki, T. Setoyama, T. Minegishi, T. Takata, T. Yamada, K. Domen, A Particulate Photocatalyst Water-Splitting Panel for Large-Scale Solar Hydrogen Production, *Joule*, Vol.2, 2018, pp. 509–520.

[61] N. Tanihara, S. Nakanishi, T. Yoshinaga, Gas and Vapor Separation Through Polyimide Membranes, *Journal of the Japan Petroleum Institute,* Vol.59, 2016, pp. 276–282.

[62] M. Pagliaro, Preparing for the Future: Solar Energy and Bioeconomy in the United Arab Emirates, *Energy Science & Engineering,* Vol.7, 2019, pp. 1451–1457.

[63] A. Boretti, S. Castelletto, S. Al-Zubaidy, Concentrating Solar Power Tower Technology: Present Status and Outlook, *Nonlinear Engineering,* Vol.8, 2019, pp. 10–31.

[64] Q. Wang, T. Hisatomi, Q. Jia, H. Tokudome, M. Zhong, C. Wang, Z. Pan, T., Takata, M. Nakabayashi, N., Shibata, Y. Li, I. D. Sharp, A. Kudo, T. Yamada, K. Domen, Scalable Water Splitting on Particulate Photocatalyst Sheets with a Solar-to-Hydrogen Energy Conversion Efficiency Exceeding 1%, *Nature Materials*, 2016, pp. 611–615.

[65] S. Chen, W. Wang, Y. Hou, Y. Hao, Y. Zhao, S. Wang, J. Meng, H. Xu, Co_3O_4 Nanosheet/g-C_3N_4 Hybrid Photocatalysts for Promoted H_2 Evolution, *ACS Applied Nano Materials*, Vol.6, No.10, 2023, pp. 8717–8725.

[66] I. Hasan, F. A. Alharthi, Synthesis of Cobalt Oxide (Co_3O_4) Nanoparticles for Efficient Photocatalytic Water Splitting and Hydrogen Production, *Chemistry Select*, Vol.8, No.34, 2023, e202302685.

[67] L. Yang, J. Liu, L. Yang, M. Zhang, H. Zhu, F. Wang, J. Yin, Co_3O_4 Imbedded g-C_3N_4 Heterojunction Photocatalysts for Visible-Light-Driven Hydrogen Evolution, *Renewable Energy*, Vol.145, 2020, pp. 691-698.

[68] R. He, H. Liang, C. Li, J. Bai, Enhanced Photocatalytic Hydrogen Production over Co_3O_4@g-C_3N_4 p-n Junction Adhering on One-Dimensional Carbon Fiber, *Colloids and Surfaces A: Physicochemical and Engineering Aspects*, Vol.586, 2020, 124200.

[69] M. Riazian, Photocatalytic Activity and Nano Structural Investigation on Co_3O_4 Nanoparticles, *Nanochemistry Research*, Vol.5, No.1, 2020, pp. 46-58.

[70] X. Yan, L. Tian, M. He, X. Chen, Three-Dimensional Crystalline/Amorphous Co/Co_3O_4 Core/Shell Nanosheets as Efficient Electrocatalysts for the Hydrogen Evolution Reaction, *Nano Letters*, Vol.15, No.9, 2015, pp. 6015–6021.

[71] P. B. Koli, K. H. Kapadnis, U. G. Deshpande, M. R. Patil, Fabrication and Characterization of Pure and Modified Co_3O_4 Nanocatalyst and their Application for Photocatalytic Degradation of Eosine Blue Dye: A Comparative Study, *Journal of Nanostructure in Chemistry*, Vol.8, 2018, pp. 453–463.

[72] D. Letsholathebe, F.T. Thema, K. Mphale, H.E.A. Mohamed, K.J. Holonga, R. Ketlhwaafetse, S. Chimidza, Optical and Structural Stability of Co_3O_4 Nanoparticles for Photocatalytic Applications, *Materials Today: Proceedings*, Vol.36, Part 2, 2021, pp. 499-503.

[73] C. Indira Priyadharsini, G. Marimuthu, T. Pazhanivel, P. M. Anbarasan, V. Aroulmoji, V. Siva & L. Mohana, Sol–Gel Synthesis of Co_3O_4 Nanoparticles as an Electrode Material for Supercapacitor Applications, *Journal of Sol-Gel Science and Technology*, Vol.96, 2020, pp. 416–422.

[74] Z. Li, R. Guo, Z. Lin, X. Ji, Y. Yuan, L. Hong, W. Pan, *Facile Synthesis of Co_3O_4 Nanoparticles with Different Morphology for Efficient Water Oxidation in Alkaline Media*, Journal of Physics: Conference Series: 2263 012013, Volume 2263, The 3rd International Conference on Advanced Material and Clean Energy 25/03/2022 - 27/03/2022, Sanya, China.

[75] İ. Kalkan, B. Kesin, M. Konuk, A. Koca, Enhancing the Photocatalytic Hydrogen Production Performances of Co_3O_4-xSx Nanoparticles with Sulfur Content Optimization, *Inorganic Chemistry Communications*, 2026, 116597.

[76] S. Sekar, V. Preethi, S. Saravanan, D. Y. Kim, S. Lee, Excellent Photocatalytic Performances of Co_3O_4–AC Nanocomposites for H_2 Production via Wastewater Splitting, *Chemosphere*, Vol.286, Part 2, 2022, 131823.

[77] J. Ji, K. Deng, J. Li, Z. Zhang, X. Duan, H. Huang, In Situ Transformation of 3D Co_3O_4 Nanoparticles to 2D Nanosheets with Rich Surface Oxygen Vacancies to Boost Hydrogen

Generation from $NaBH_4$, *Chemical Engineering Journal*, Vol.424, 2021, 130350.

[78] A. Anil, B. Festo, K. Thaju C. Bhagya, S. Muhammadhu A. Shibli, Active Co_3O_4 Nanosheet Integration and Morphological Tuning of Ni Nanocones for Efficient Electrocatalytic Hydrogen Generation, *ACS Applied Engineering Materials*, Vol.4, No.2, 2026, pp. 717–728.

[79] H. Ardeshirfard, D. Elhamifar, An Efficient Method for the Preparation of Magnetic Co_3O_4 Nanoparticles and the Study of their Catalytic Application, *Frontiers in Catlaysis, Special Section: Heterogeneous Catalysis*, Vol.3, 2023.

[80] O. M. Mohammed, A. Naghipour, S. T. Fardood, Green Synthesis, Characterization and Photocatalytic Activity of Co_3O_4 Nanoparticles, *Materials Advances*, Vol.5, 2024, pp. 8111-8131.

[81] M. Salavati-Niasari, A. Khansari, F. Davar, Synthesis and Characterization of Cobalt Oxide Nanoparticles by Thermal Treatment Process, *Inorganica Chimica Acta*, Vol.362, No.14, 2009, pp. 4937-4942.

[82] O. Mahmood, M. Ali, N. Saeid, T. Fardood, Green Synthesis, Characterization and Photocatalytic Activity of Co_3O_4 Nanoparticles, *Nanochemistry Reseacrh*, Vol.10, No.2, 2025, 233-239.

[83] B. Meenatchi, V. Sathiya Lakshmi, A. Manikandan, V. Renuga, A. Sharmila, K. R. Nandhine Deve, S. Kumar Jaganathan, Protic Ionic Liquid Assisted Synthesis and Characterization of Ferromagnetic Cobalt Oxide Nanocatalyst, *Journal of Inorganic and Organometallic Polymers and Materials*, Vol.27, 2017, pp. 446–454.

[84] Ravina, G. Srivastava, S. Dalela, S. Kumar, M. Nasit, J. Singh, M. Ayaz Ahmad, P. A. Alvi, Study of Structural, Optical, Surface and Electrochemical Properties of Co_3O_4 Nanoparticles for Energy Storage Applications, *Interactions*, Vol.245, 2024, article number 85.

[85] N. O. M. Dewi, Y. Yulizar, D. O. B. Apriandanu, Green Synthesis of Co_3O_4 Nanoparticles Using Euphorbia Heterophylla L. Leaves Extract: Characterization and Photocatalytic Activity, *13th Joint Conference on Chemistry (13th JCC), IOP Conf. Series: Materials Science and Engineering*, Vol.509, 2019, 012105, pp. 1-8.

[86] X. Wang, X. Chen, L. Gao, H. Zheng, Z. Zhang, Y. Qian, One-Dimensional Arrays of Co_3O_4 Nanoparticles: Synthesis, Characterization, and Optical and Electrochemical Properties, *The Journal of Physical Chemistry B*, Vol.108, No.42, 2004, pp. 16401–16404.

[87] N. A. M. Barakat, M. S. Khil, F. A. Sheikh, H.Y. Kim, Synthesis and Optical Properties of Two Cobalt Oxides (CoO and Co_3O_4) Nanofibers Produced by Electrospinning Process, *The Journal of Physical Chemistry C*, Vlol.112, No.32, 2008, pp. 12225–12233.

[88] M. R. M. Shafiee, J. Parhizkar, S. Radfar, Removal of Rhodamine B by g-C_3N_4/Co_3O_4/MWCNT Composite Stabilized in Hydrogel via the Synergy of Adsorption and Photocatalysis under Visible Light, *Journal of Materials Science: Materials in Electronics*, Vol.30, 2019, pp. 12475–12486.

[89] E. W. Slessarev, J. P. Schimel, Partitioning Sources of CO_2 Emission after Soil Wetting using High-Resolution Observations and Minimal Models, *Soil Biology and Biochemistry*, Vol.143, 2020, 107753.

[90] R. Bhargava; S. Khan; N. Ahmad; M. Mohsin N. Ansari, Investigation of Structural, Optical and Electrical Properties of Co_3O_4 Nanoparticles, *AIP Conference Proceedings*, Vol.1953, No.1, 2018.

[91] V. D. Dang, N. T. H. Nhung, I. Rabani, N. T. Tran, B. T. P. Thuy, H. B. Truong, Advances in Co_3O_4 Nanomaterial-Based Photocatalysts for Water Purification: Mechanisms, Green Synthesis, Activation of Oxidants, Waste Derived Sources, and Computational Insights, *RSC Advances*, Vol.15, No.19088, 2025, pp. 1-16.

[92] L. Wang, Q. Zeng, X. Gao, Y. Wei, W. Li, D. Zeng, Rational Design of Co_3O_4 Nanosheet/ZnCdS Nanoparticle Heterojunctions for Optimized Photocatalytic Hydrogen Generation, *International Journal of Hydrogen Energy*, Vol.92, 2024, pp. 1133-1142.

[93] A. B. Vennela, D. Mangalaraj, N. Muthukumarasamy, S. Agilan, K. V. Hemalatha, Structural and Optical Properties of Co_3O_4 Nanoparticles Prepared by Sol-gel Technique for Photocatalytic Application, *International Journal of Electrochemical Science,* Vol.14, 2019, pp. 3535 – 3552.

[94] S. N. Karthick, K. V. Hemalatha, C. Justin Raj, H. J. Kim, M. Yi, Synthesis of Nano-Bound Microsphere Co_3O_4 by Simple Polymer-Assisted Sol-Gel Technique, *Journal of Nanoparticle Research*, Vol.15, No.3, article id.1474, pp. 1-13.

[95] L.H. Hu, K.Q. Sun, Q. Peng, B.Q. Xu and Y.D. Li, Surface Active Sites on Co_3O_4 Nanobelt and Nanocube Model Catalysts for CO Oxidation, *Nano Research*, Vol.3, 2010, pp. 363-368.

[96] K. Agilandeswari, A. Rubankumar, Synthesis, Characterization, Optical, and Magnetic Properties of Co_3O_4 Nanoparticles by Quick Precipitation, *Synthesis and Reactivity in*

Inorganic, Metal-Organic, and Nano-Metal Chemistry, Vol.46, 2016, pp. 502–506.

[97] P. Gowthami, A. Kosiha, S. Meenakshi, G. Boopathy, A. G. Ramu, D.n Choi, Biosynthesis of ¬Co_3O_4 Nanomedicine by using Mollugo oppositifolia L. Aqueous Leaf Extract and Its Antimicrobial, Mosquito Larvicidal Activities, *Scientific Reports*, Vol.13,| 2023, 9002.

[98] A. Kaur, S. Kumar, H. Kaur, G. S. Lotey, P. P. Singh, G. Singh, Supreet, S. Kumar, J. Dalal, G. Bouzid, M. Misra, R. Pandey, S. Kausha, Enhanced Photocatalytic Degradation and Antimicrobial Activities of Biogenic Co_3O_4 Nanoparticles Mediated by Fenugreek: Sustainable Strategies, *Advanced Materials*, Vol.5, 2024, pp. 8111-8131.

[99] M. Sappani Muthu, P. Ajith, J. Agnes, M. S. Selvakumar, M. Presheth, D. Prem Anand, Hydrothermal synthesis and characterisation of nano graphene oxide/cobalt oxide (GO/Co3O4) nanocomposite suitable for supercapacitor applications, *Journal of Materials Science: Materials in Electronics*, Vol.34, 2023, article number 1766.

[100] A. S. Sathappan, K. Madhivanan, R. Atchudan, S. Arya, A. K. Sundramoorthy, Electrochemical Detection of Paracetamol with a Polypyrrole-Cobalt Oxide Nanocomposite Modified Sensor, *ECS Journal of Solid State Science and Technology*, Vol.14, No.2, 2025, 027001.

[101] H. Ardeshirfard, D. Elhamifar, An efficient method for the preparation of magnetic Co3O4 nanoparticles and the study of their catalytic application, *Sec. Heterogeneous Catalysis*, Vol.3, 2023, 1194977.

[102] Y. Georgiou, M. Smyrnioti, T. Ioannides, Co3O4 Catalysts for Complete Toluene Oxidation: Review including Meta-Analysis of Catalyst Activity Data, *Catalysts*, Vol.13, No.11, 2023, 1454.

[103] S. Elbasuney, S. Ismael, M. Yehia, H. Tantawy, A. Saleh, S. M. Abdelkhalek, G. S. El-Sayyad, Facile Synthesis and Catalytic Activity Assessment of Cobalt Oxide Nanoparticles: Towards Advanced Energetic Nitramines, *Journal of Cluster Science*, Vol.34, 2023, pp. 2579–2590.

[104] H. Chen, M. Yang, Y. Liu, J. Yue, G. Chen, Influence of Co3O4 Nanostructure Morphology on the Catalytic Degradation of p-Nitrophenol, *Molecules*, Vol.28, No.21, 2023, 7396.

[105] J. Sun, M. Li, H. Liu, L. Guo, X. Dong, C. Liang, Transmission electron microscopy analysis of Co3O4 degradation induced by electron irradiation, *Micron*, Vol.190, 2025, 103786.

[106] G. Rathika, V. Suba, D. Shanthana Lakshmi & Roopala Rani, Exploring the Biosynthesized Metal Nanoparticles for their Catalytic Degradation of Toxic Water Wastes and Antimicrobial Potential, *Journal of Inorganic and Organometallic Polymers and Materials*, Vol.32, 2022, pp. 3153–3169.

[107] V. D. Dang, N. T. H. Nhung, I. Rabani, N. T. Tran, B. T. P. Thuy, H. B. Truong, Advances in Co_3O_4 Nanomaterial-Based Photocatalysts for Water Purification: Mechanisms, Green Synthesis, Activation of Oxidants, Waste-Derived Sources, and Computational Insights, *RSC Advances*, Vol.15, No.24, 2025, pp. 19088–19103.

[108] T. Takata, J. Jiang, Y. Sakata, M. Nakabayashi, N. Shibata, V. Nandal, K. Seki, T. Hisatomi, K. Domen, Photocatalytic Water Splitting with Quantum Efficiency of Almost Unity, *Nature*, Vol.581, 2020, pp. 411–414.

[109] P. Peñas, P. van der Linde, W. Vijselaar, D. van der Meer, D. Lohse, J. Huskens, H. Gardeniers, M. A. Modestino, D. F. Rivas, Decoupling Gas Evolution from Water-Splitting Electrodes, *Journal of The Electrochemical Society*, Vol.166, 2019, pp. H769–H776.

[110] J. Cai, C. Cheng, B. Liu, J. Zhang, C. Jiang, B. Cheng, CdS/DBTSO-BDTO S-Scheme Photocatalyst for H_2 Production and Its Charge Transfer Dynamics, *Acta Physico-Chimica Sinica*, Vol.41, No.8, 2025, 100084.

[111] L. Supramaniam, S.-M. Lam, J.-C. Sin, P. Lahijani, A. R. Mohamed, Recent Advances in Hydrogen Production by Solar Photoreforming of Plastic Feedstocks using Nanocatalytic Materials: A Review, *International Journal of Hydrogen Energy*, Vol.145, 2025, pp. 95-118.

[112] Y. Dong, B. Liu, M. He, Z. Zhang, C. Tang, J. Zhao, H. Wu, Y. Fan, W. Ma, Microwave-Coupled Recycling of Plastic Waste into Hydrogen and Carbon Nanotubes over Economical Iron-Based Catalyst, *International Journal of Hydrogen Energy*, Vol.115, 2025, pp. 24-36.

[113] R. Li, F. Wang, F. Lv, P. Wang, X. Guo, J. Feng, D. Li, Y. Chen, Simultaneous Hydrogen Production and Conversion of Plastic Wastes into Valued Chemicals over a Z-Scheme Photocatalyst, *International Journal of Hydrogen Energy*, Vol.51, Part C, 2024, pp. 406-414.

[114] T.-M. Tien, E. L. Chen, A Novel ZnO/Co_3O_4 Nanoparticle for Enhanced Photocatalytic

Hydrogen Evolution under Visible Light Irradiation, *Catalysts*, Vol.13, No.5, 2023, 852.

[115] I. Hasan, F. A. Alharthi, Synthesis of Cobalt Oxide (Co_3O_4) Nanoparticles for Efficient Photocatalytic Water Splitting and Hydrogen Production, *Chemistry Select*, Vol.8, No.34, 2023, e202302685.

[116] U. Farooq, M. E. Khan, A. Mohammad, N. Hasan, A. A. Alamri, M. Sharma, Sustainable Synthesis of Copper Oxide Nanoparticles: Data-Driven Photocatalysis, Pt-Free Hydrogen Production, and Antibacterial Assessment, *Catalysts*, Vol.15, No.12, 2025, 1163.

[117] C. Xu, W. Zhang, J. Tang, C. Pan, G. Yu, Porous Organic Polymers: An Emerged Platform for Photocatalytic Water Splitting, *Frontiers in Chemistry, Specific Section: Catalysis and Photocatalysis*, Vol.6 – 2018, article 592, pp. 1-12.

[118] P. Guo, S. Sun, H. Sun, Y. Tian, Y. Zhang, P. Zhao, B. Liu, G. Yue, Z. Li, Influences of Polymer Synthesis on the Photocatalytic Hydrogen Production of Porous Organic Frameworks, *Journal of Photochemistry and Photobiology A: Chemistry*, Vol.478, 2026, 117217.

[119] P. T. Poojitha, R. Dhanalakshmi, M. R. Karim, S. J. An, K. M. Rao, S. P. R. Mallem, Y. L. Kim, Effective CdS:(Ce, Ga) Nanoparticles for Photocatalytic H_2 Production Under Artificial Solar Light Exposer, *Journal of Composites Science*, Vol.9, No.1, 2025, 34.

[120] B. Han, S. Liu, N. Zhang, Y. Z. Xu, Z. R. Tang, One-Dimensional CdS@ MoS_2 Core-Shell Nanowires for Boosted Photocatalytic Hydrogen Evolution under Visible Light, *Applied Catalysis B: Environmental*, Vol.202, 2017, pp. 298–304.

[121] X. L. Yin, L. L. Li, W. J. Jiang, Y. Zhang, X. Zhang, L. J. Wan, J. S. Hu, MoS_2/CdS Nanosheets-on-nanorod Heterostructure for Highly Efficient Photocatalytic H_2 Generation under Visible Light Irradiation, *ACS Applied Materials & Interfaces*, Vol.8, 2016, pp. 15258–15266.

[122] K. Chen, J. Liu, Z. Huang, S. Zong, L. Liu, W. Tan, Construction of Novel 2D-0D $MnPS_3$–$Cs_4W_{11}O_{35}$ Composite for the Improved Photocatalytic Hydrogen Evolution Activity, *International Journal of Hydrogen Energy*, Vol.46, 2021, pp. 33823–33834.

[123] M. Kaykhaii, Z. Honarmandrad, J. Gębicki, Effect of Microplastics Pollution on Hydrogen Production from Biomass: A Comprehensive Review, *Industrial & Engineering Chemistry Research*, Vol.62, 2023, pp. 3835−3843.

[124] R. K. Soni, S. Soam, K. Dutt, Studies on Biodegradability of Copolymers of Lactic Acid, Terephthalic Acid and Ethylene Glycol, *Polymer Degradation and Stability*, Vol.94, 2009, pp. 432-437.

[125] N. Karthikeyan, J. Joseph Prince, S. Ramalingam, S. Periandy, Electronic [UV–Visible] and Vibrational [FT-IR, FT-Raman] Investigation and NMR–Mass Spectroscopic Analysis of Terephthalic Acid using Quantum Gaussian Calculations, *Spectrochimica Acta, Part A: Molecular and Biomolecular Spectroscopy*, Vol.139, 2015, pp. 229-242.

[126] Y. Han, Z. Wang, X. Yang, Z. Li, Y. Li, In Situ Reinforced g-C_3N_4/CoO/CoP Ternary Composite for Enhanced Photocatalytic H_2 Production, *Catalysts*, Vol.15, 2025, 315.

[127] J. Lin, K. Hu, Y. Wang, W. Tian, T. Hall, X. Duan, H. Sun, H. Zhang, E. Cortés, S. Wang, Tandem Microplastic Degradation and Hydrogen Production by Hierarchical Carbon Nitride-Supported Single-Atom Iron Catalysts, *Nature Communications*, Vol.15, 2024, 8769.

[128] P. Praus, L. Řeháčková, M. Filip-Edelmanová, A. Gavlová, M. Koštejn, R. Škuta, J. Bednárek, P. Bednář, K. Kočí, Photoreforming of PET and PLA Microplastics for Sustainable Hydrogen Production using TiO_2 and g-C_3N_4 Photocatalysts, *Journal of Environmental Chemical Engineering*, Vol.13, No.3, 2025, 116998.

[129] G. V. Buxton, C. L. Greenstock, W. P. Helman, A. B. Ross, Critical Review of Rate Constants for Reactions of Hydrated Electrons, Hydrogen Atoms and Hydroxyl Radicals ($OH^\bullet/O^{-\bullet}$ in Aqueous Solution, *Journal of Physical and Chemical Reference Data*, Vol.17, No.2, 1988, pp. 513-886.

[130] H.-Y. Ren, X.-W. Wang, F. Kong, L. Zhao, D. Xing, N.-Q. Ren, B.-F. Liu, Enhanced Semi-Continuous Hydrogen Production by Addition of Microplastics under Mesophilic and Thermophilic Fermentation, *Fuel*, Vol.315, 2022, 123247.

[131] M. Wang, Y. Chu, F. Meng, J. Zhao, H. Zhang, S. Wang, J. Zhang, Enhancing Photocatalytic Hydrogen Production in Conjugated Porous Polymers through Donor-π-Donor Fragment Insertion, *International Journal of Hydrogen Energy*, Vol.79, 2024, pp. 492-502.

[132] X. Chi, Q. Chen, Z.-A. Lan, X. Zhang, X. Chen, X. Wang, Structure–Property Relationship of Cyano-Functionalized Conjugated Polymers for Photocatalytic Hydrogen Production, *Chemistry-*

A European Journal, Vol.29, No.2, 2023, e202202734.

[133] C.-L. Chang, W.-C. Lin, L.-Y. Ting, C.-H. Shih, S.-Y. Chen, T.-F. Huang, H. Tateno, J. Jayakumar, W.-Y. Jao, C.-W. Tai, C.-Y. Chu, C.-W. Chen, C.-H. Yu, Y.-J. Lu, C.-C. Hu, A. M. Elewa, T. Mochizuki, H.-H. Chou, Main-Chain Engineering of Polymer Photocatalysts with Hydrophilic Non-Conjugated Segments for Visible-Light-Driven Hydrogen Evolution, *Nature Communications,* Vol.13, 2022, Article number: 5460.

[134] X. He, W. Ma, S. Zhu, D. Li, J.-X. Jiang, The Effect of Electronic Structure Matching between Building Blocks in Conjugated Porous Polymers on Photocatalytic Hydrogen Evolution Activity, *Chinese Journal of Catalysis*, Vol.73, 2025, pp. 279-288.

[135] S. Kim, M. Kim, D. R. Lustig, G. Ham, C. Park, D. Lee, L. Steier, H. Cha, Design Strategies, Methods, and Photophysical Insights in Polymeric Photocatalysts for Solar-Driven Hydrogen Evolution, *Nano Convergence*, Vol.16, No.13, 2026, article numer:7.

[136] M. G. Mohamed, A. F. M. EL-Mahdy, M. G. Kotp, S.-W. Kuo, Advances in Porous Organic Polymers: Syntheses, Structures, and Diverse Applications, *Materials Advances*, Vol.3, 2022, pp. 707-733.

[137] L. Liu, M. A. Kochman, W. Zhao, M. A. Zwijnenburg, R. S. Sprick, Linear Conjugated Polymer Photocatalysts with Various Linker Units for Photocatalytic Hydrogen Evolution from Water, *Chemical Communications*., Vol.58, 2022, pp. 10639-10642.

[138] W. Jung, J. Choi, S. An, S. Yun, D. S. Chung, H. Cha, J. Lim, T. Park, Photocatalytic Hydrogen Evolution with Conjugated Polymers: Structure–Property Insights and Design Strategies, *Advanced Energy Materials*, Vol.15, No.39, 2025, 2501600.

Contribution of Individual Authors to the Creation of a Scientific Article (Ghostwriting Policy)

Prof. Dr. Delia Teresa Sponza and Post-Dr. Rukiye Öztekin took an active role in every stage of the preparation of this article.

The authors equally contributed in the present research, at all stages from the formulation of the problem to the final findings and solution.

Sources of Funding for Research Presented in a Scientific Article or Scientific Article Itself

The experimental phases of this research study were conducted at the National Research Council (NRC) of Canada, Research Centers, Ontario, Canada. The authors would like to thank this body for providing financial support.

Conflict of Interest

The authors have no conflicts of interest to declare that are relevant to the content of this article.

Creative Commons Attribution License 4.0 (Attribution 4.0 International, CC BY 4.0)

APPENDIX

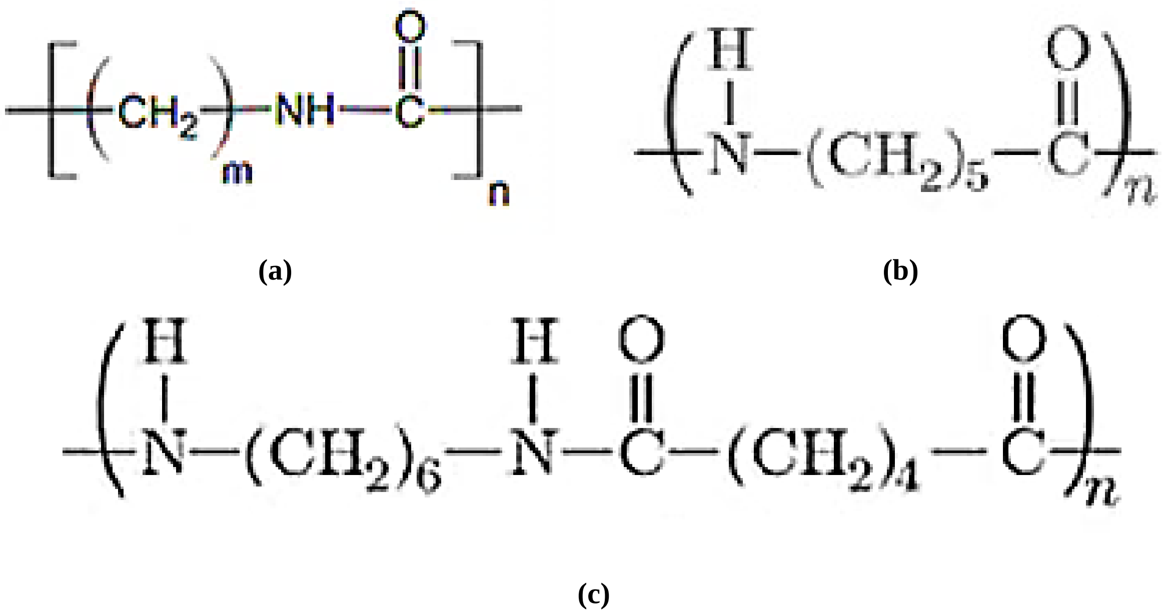

(a)

(b)

(c)

Figure 1. The chemical structure of (**a)** Polyamide (PA) MPs, (**b)** Polyamide (PA, Nylon 6) MPs, and (**c)** Polyamide (PA, Nylon 66) MPs, respectively.

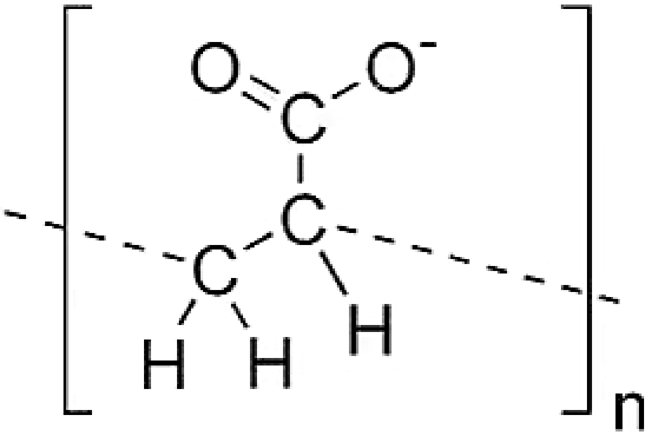

Figure 2. The general chemical structure of Polyacrylate (PAK) MPs.

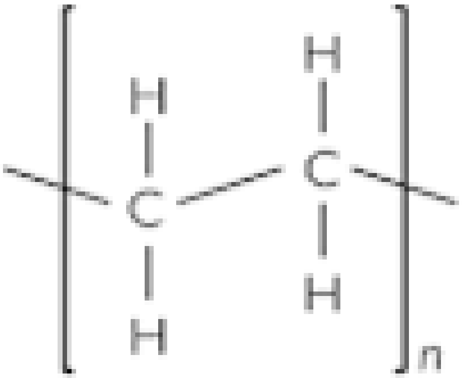

Figure 3. The general chemical structure of Polyethylene (PE) MPs.

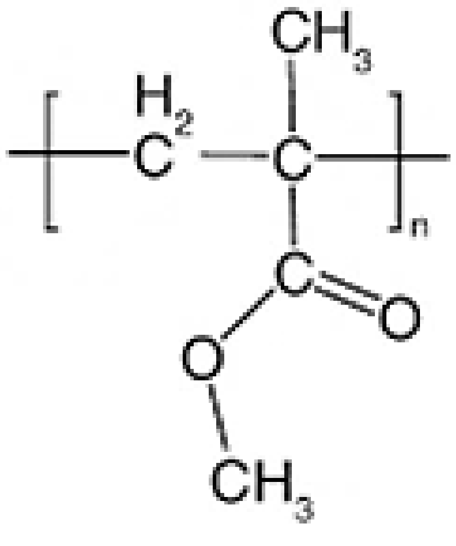

Figure 4. The general chemical structure of Polymethyl methacrylate (PMMA) MPs.

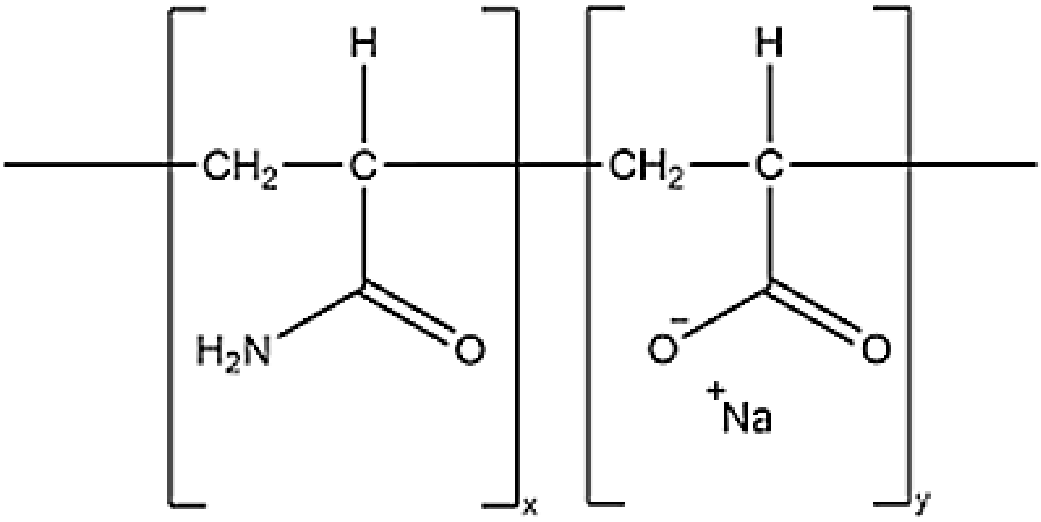

Figure 5. The general chemical structure of Acrylates Copolymer (AC) MPs.

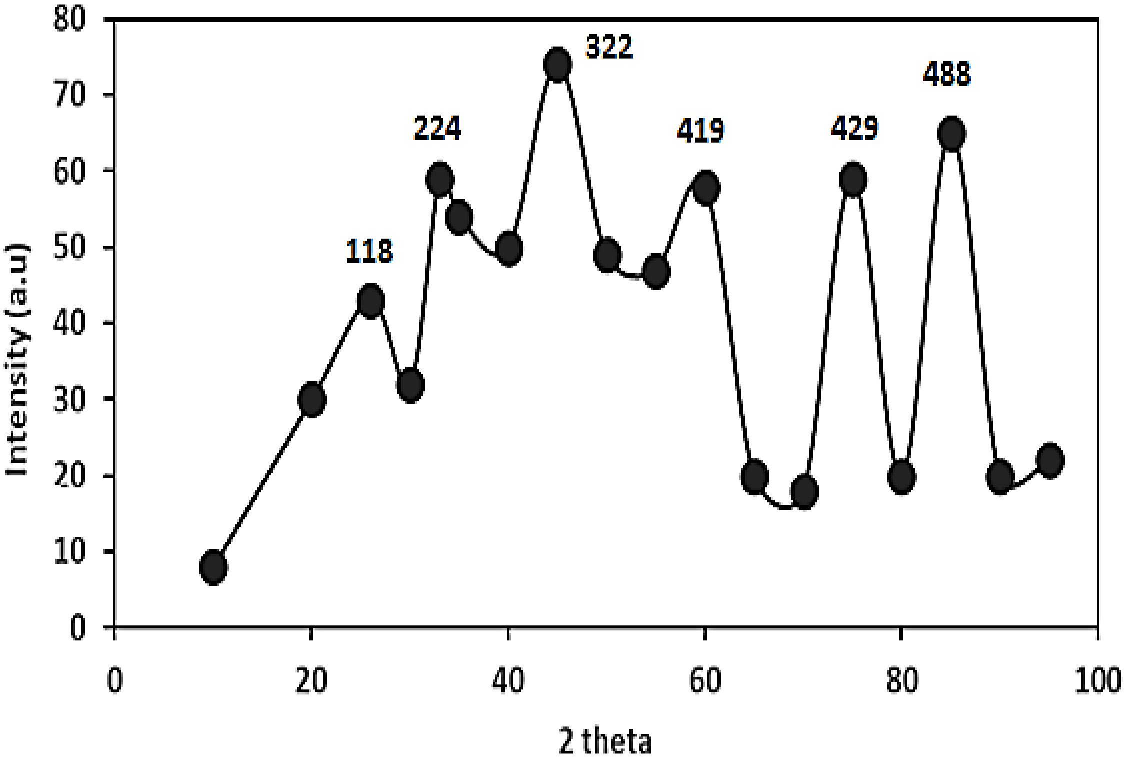

Figure 6. XRD results of Co_3O_4 NPs.

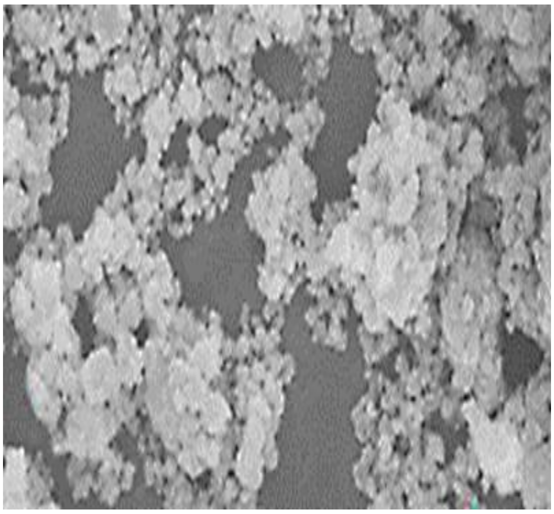

(a)

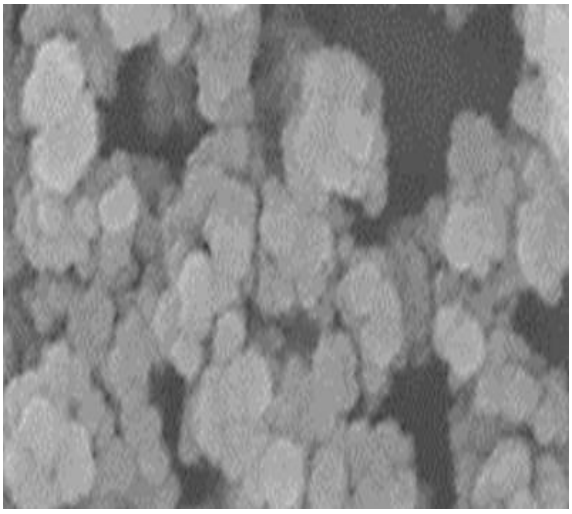

(b)

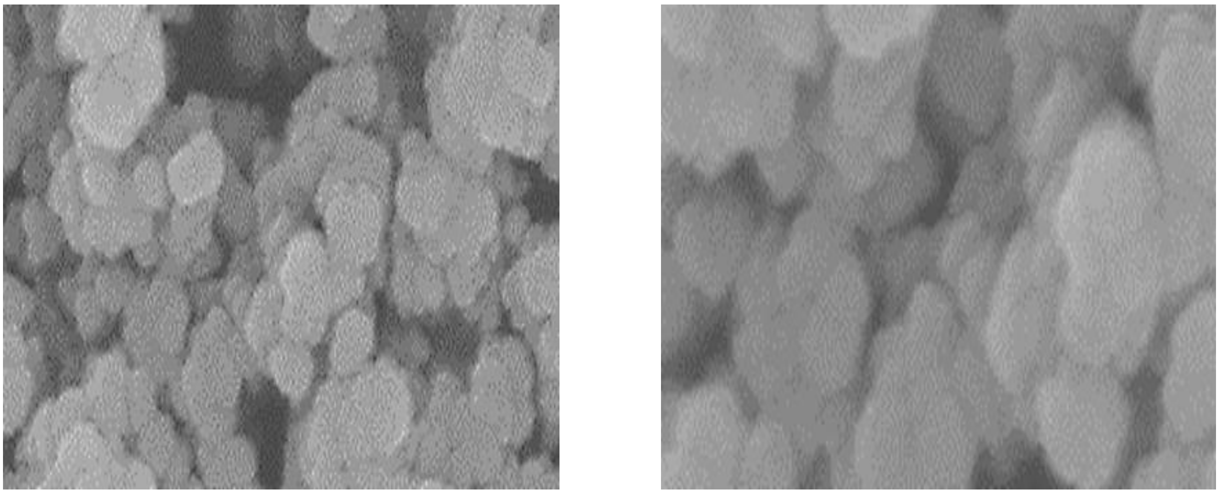

(c) **(d)**

Figure 7. SEM analysis results of **(a)** 3 nm Co_3O_4 NPs, **(b)** 100 nm Co_3O_4 NPs, **(c)** 300 nm Co_3O_4 NPs and **(d)** 500 nm Co_3O_4 NPs, respectively.

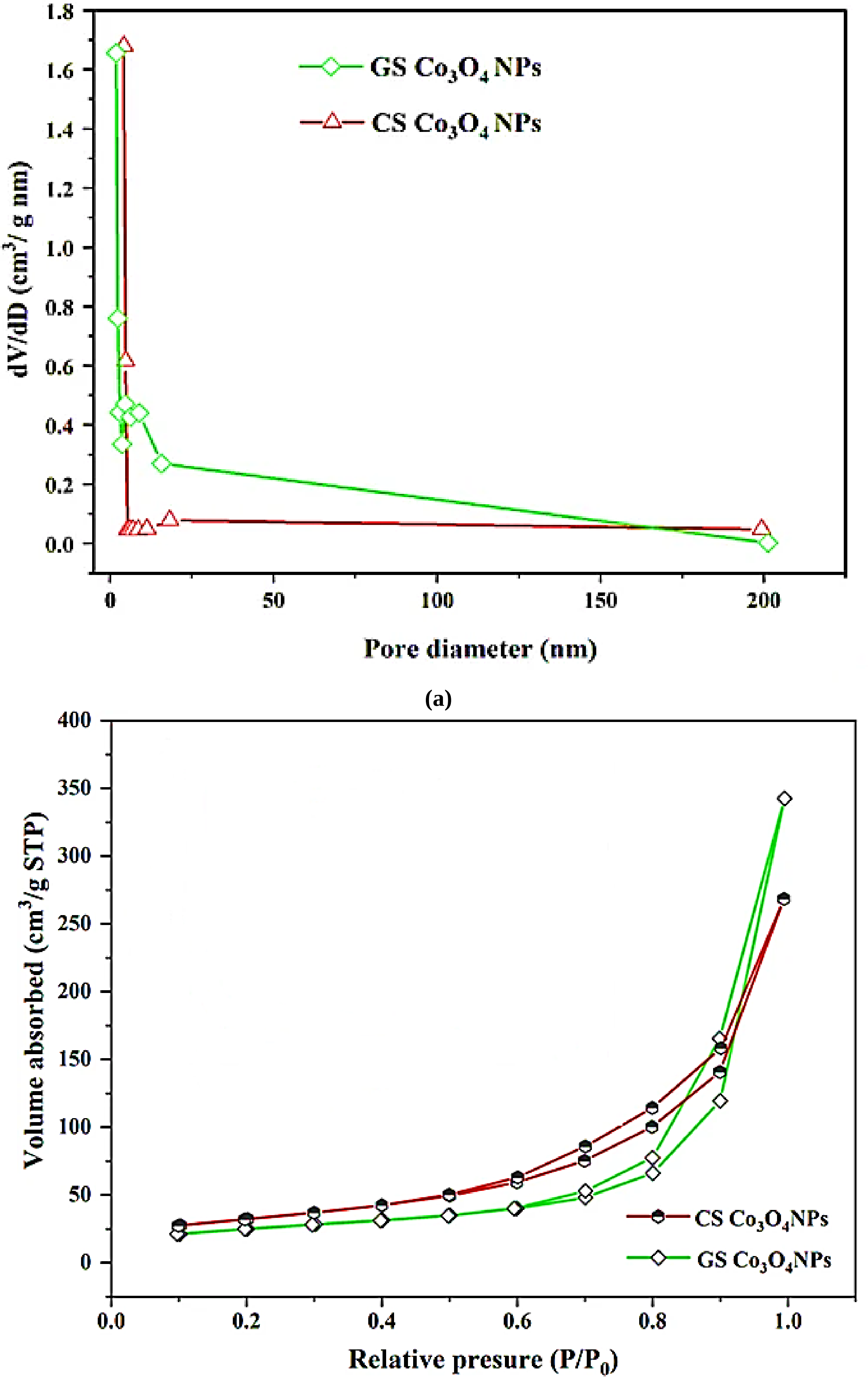

(a)

(b)

Figure 8. BET surface area pore size **(a)** and volume distribution plot **(b)** of Co_3O_4 NPs

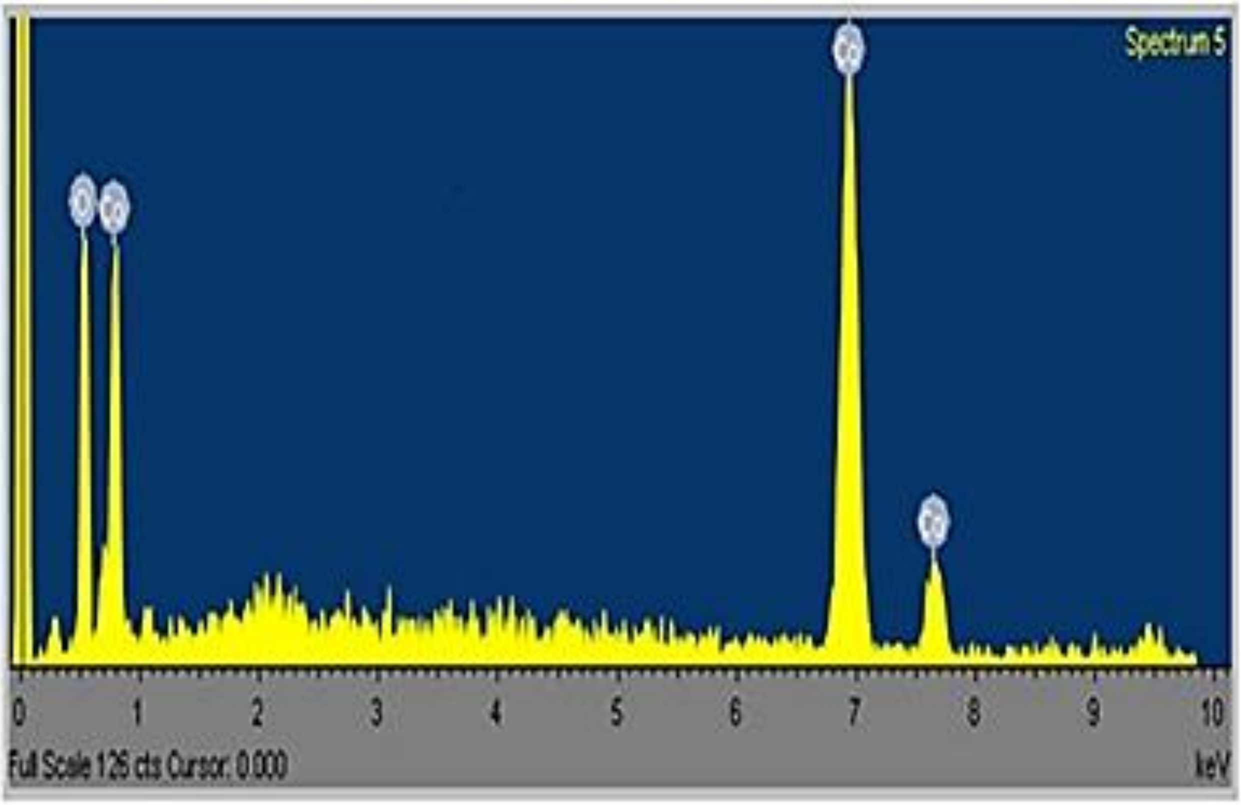

(a)

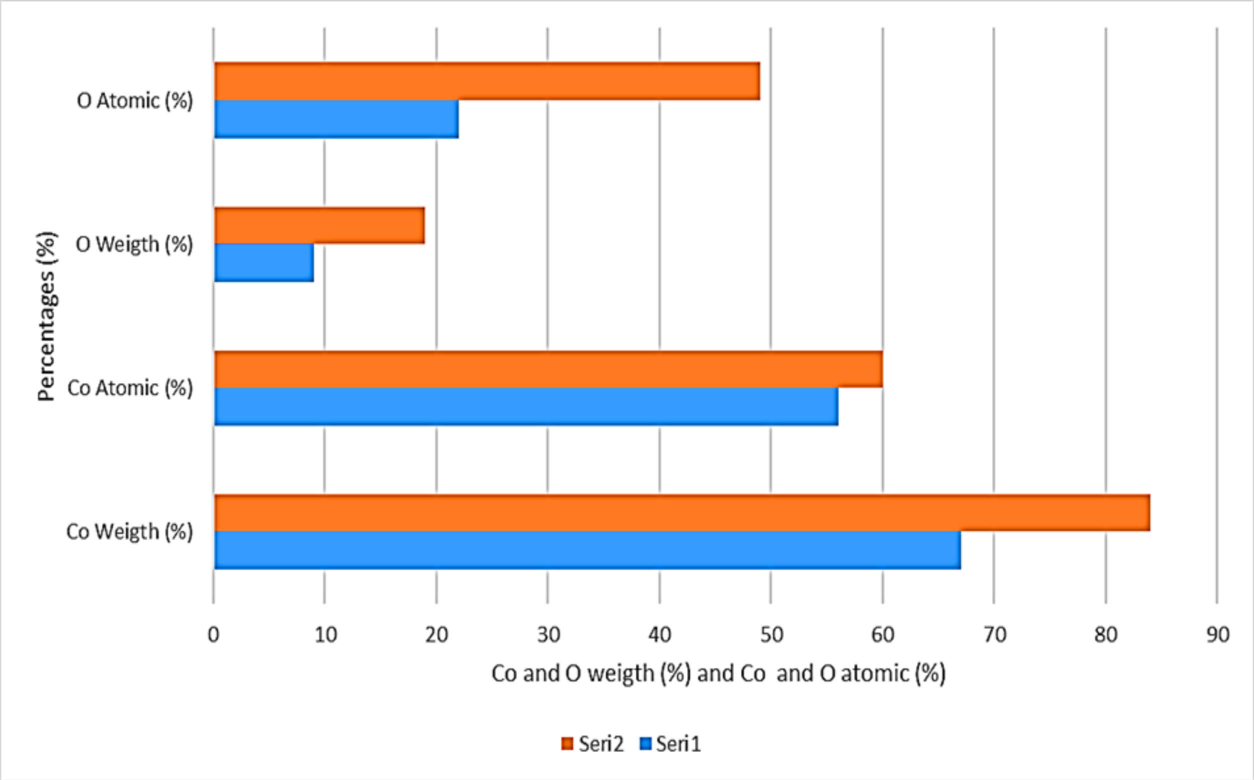

(b)

Figure 9. (**a**) The EDX spectrum of Co_3O_4 NPs, and (**b**) the presence of Co and O elements weight (%) and Co and O atomic (%) versus efficiencies (%), respectively.

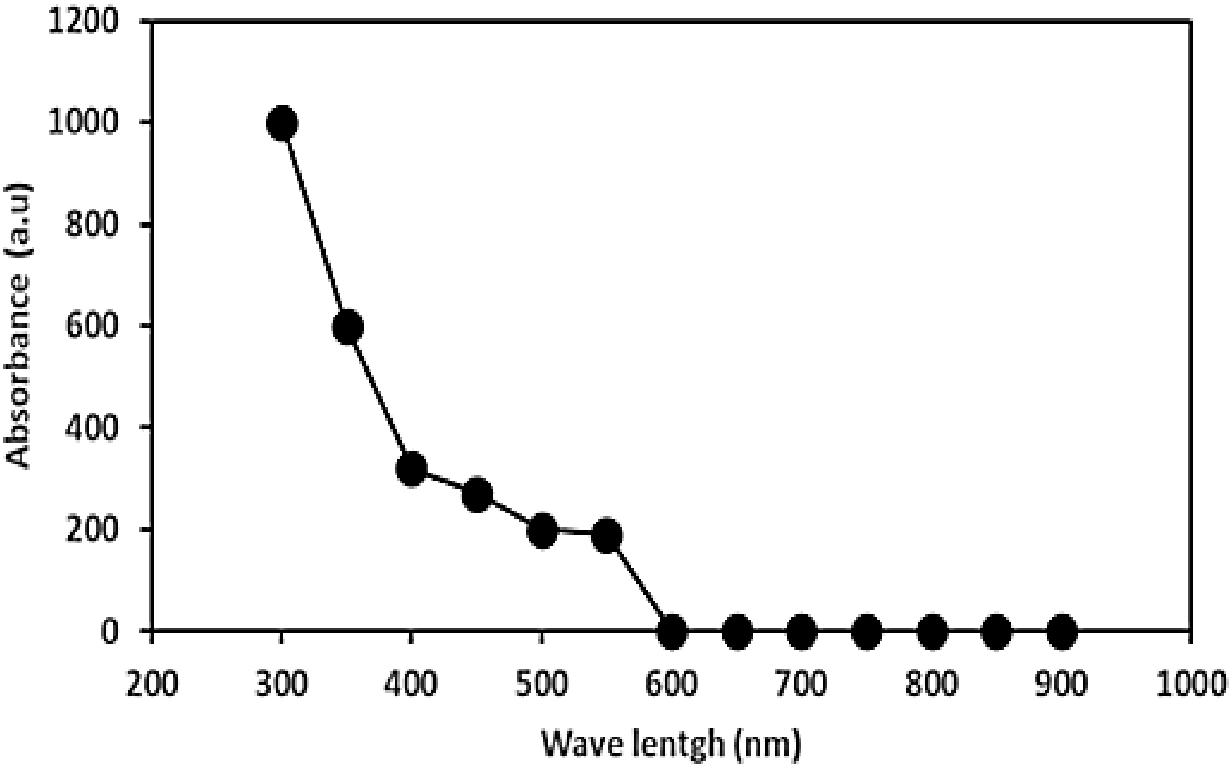

(a)

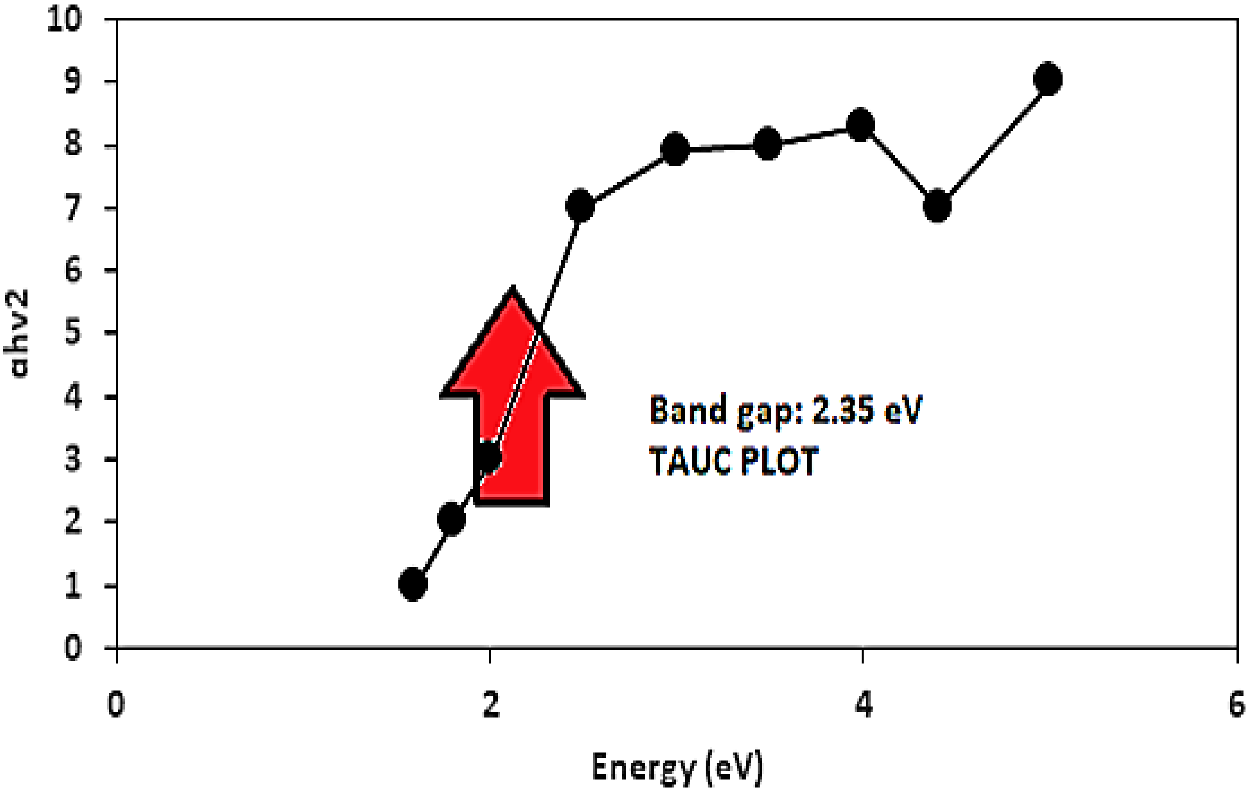

(b)

Figure 10. (a) The UV-vis absorption spectrum of Co_3O_4 NPs, and (**b**) Tauc plot of Co_3O_4 NPs, respectively.

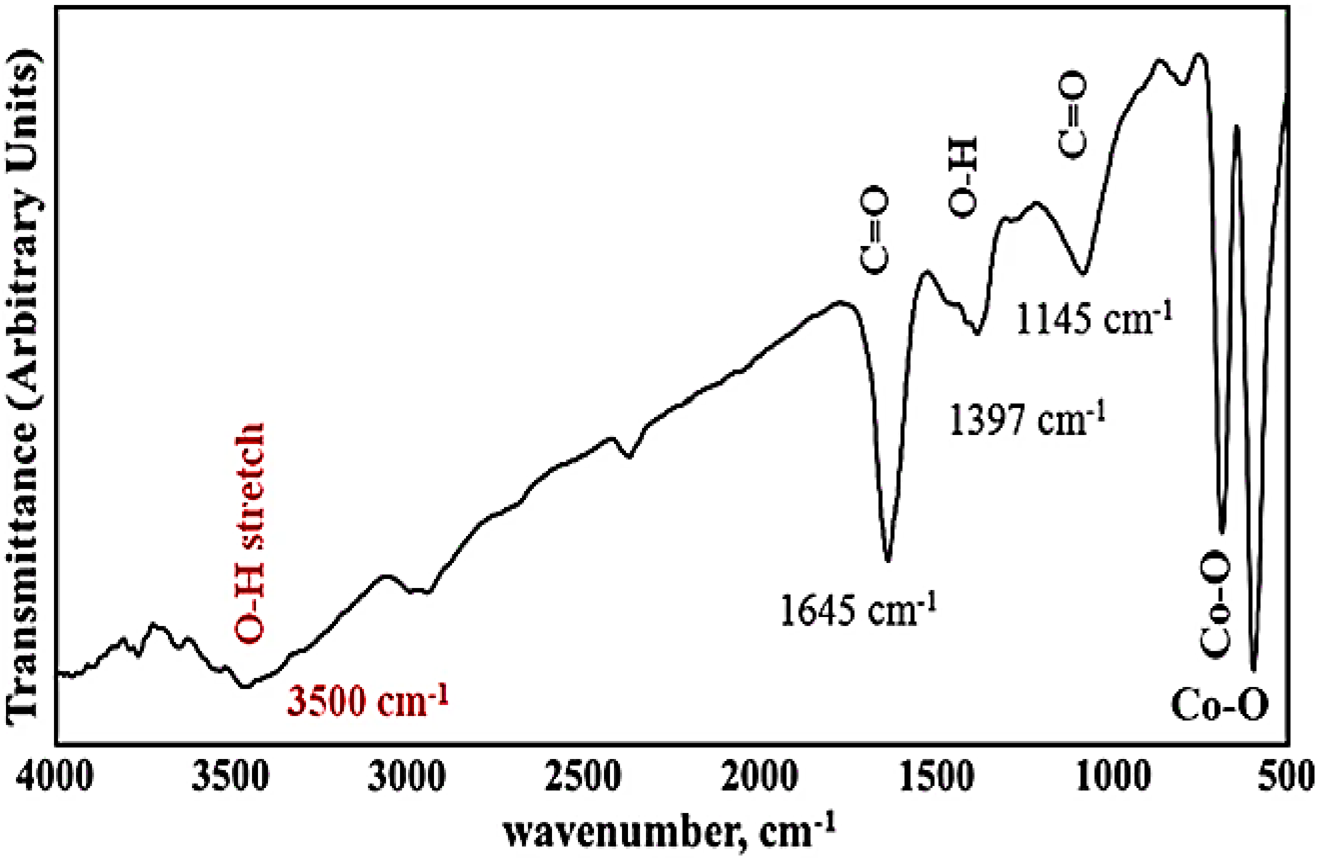

Figure 11. FTIR spectrum of Co_3O_4 NPs.

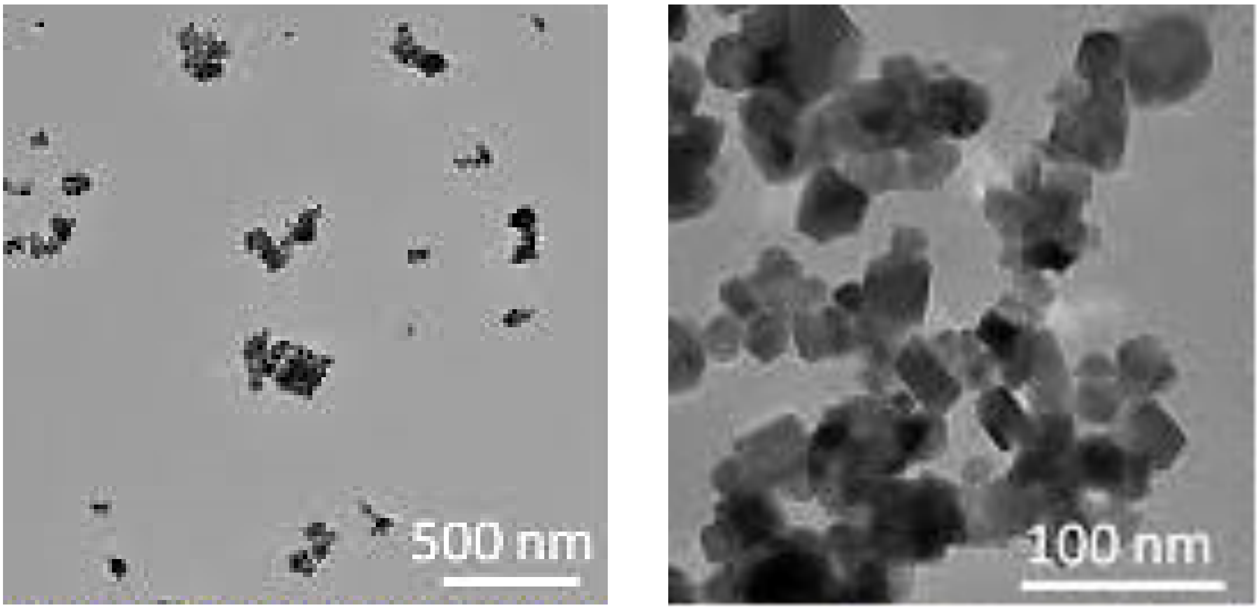

(a) **(b)**

Figure 12. HRTEM analysis results of Co_3O_4 NPs **(a)** HRTEM image size: 500 nm, and **(b)** HRTEM image size: 100 nm, respectively.

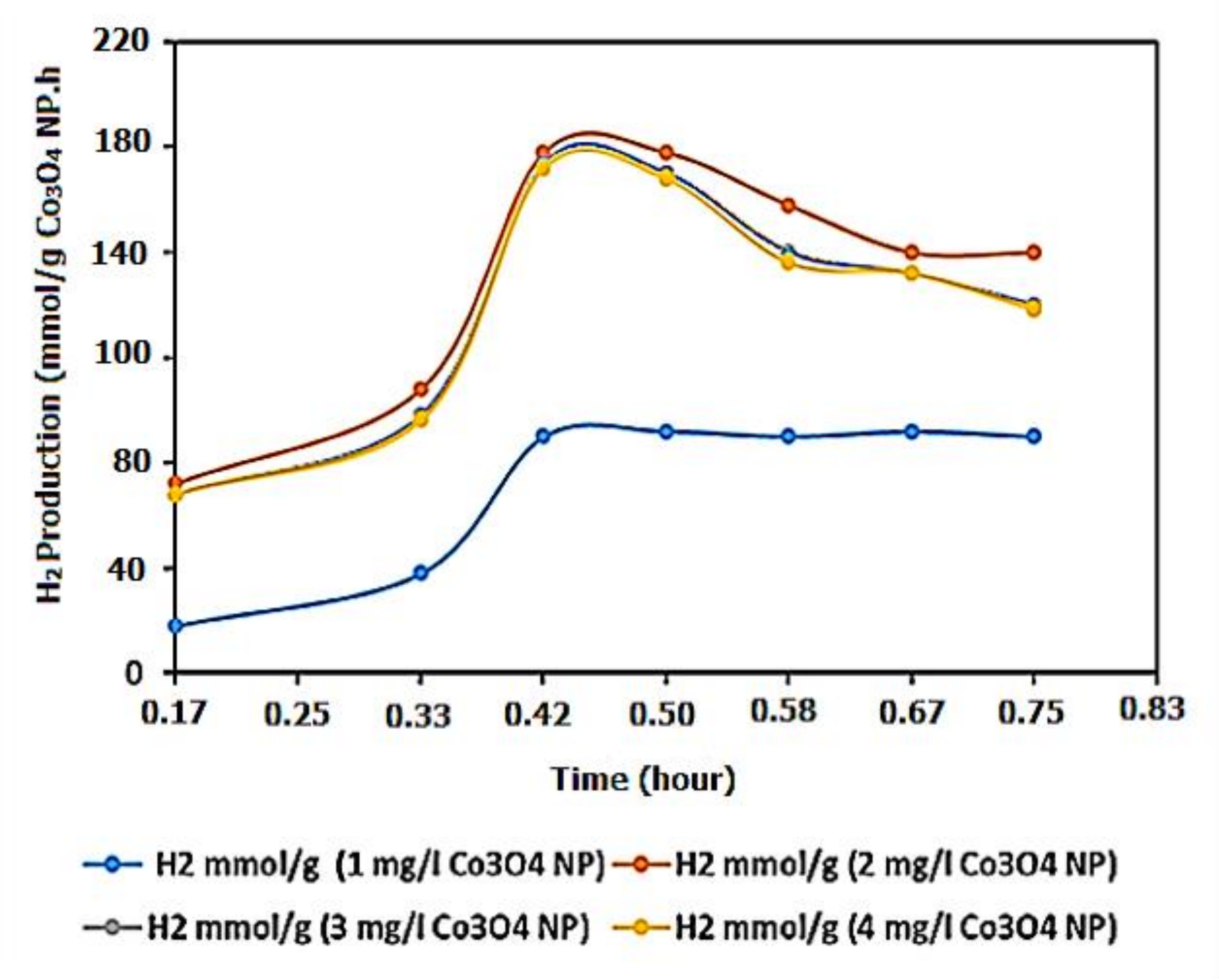

Figure 13. (a) H_2 productions in Polyamide (PA, Nylon).

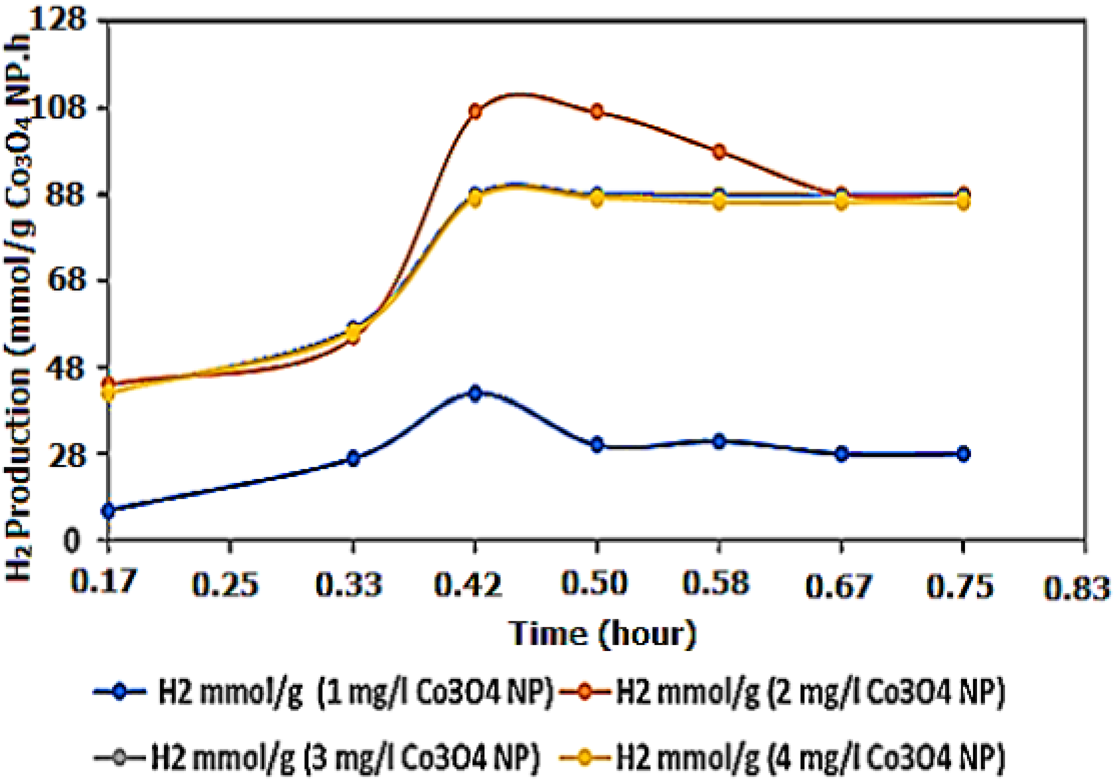

Figure 13. (b) H_2 production in Polyacrylate (PAK).

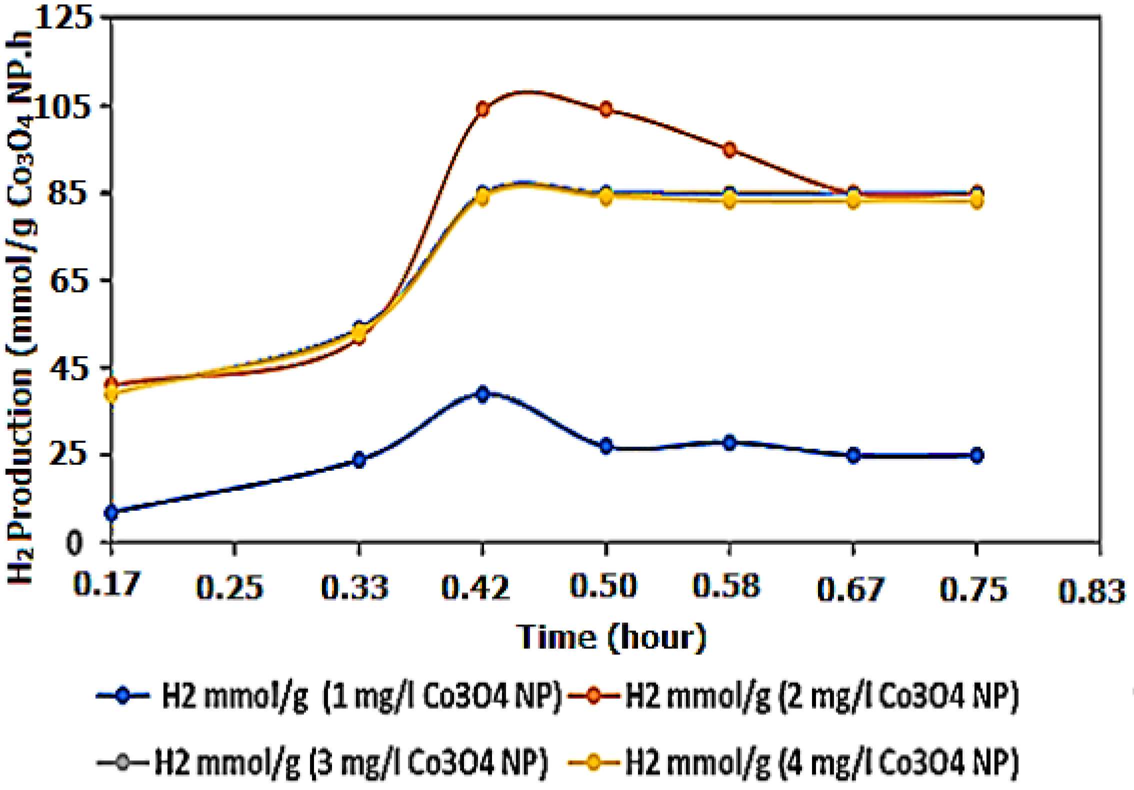

Figure 13. (c) H_2 production in Polyethylene (PE).

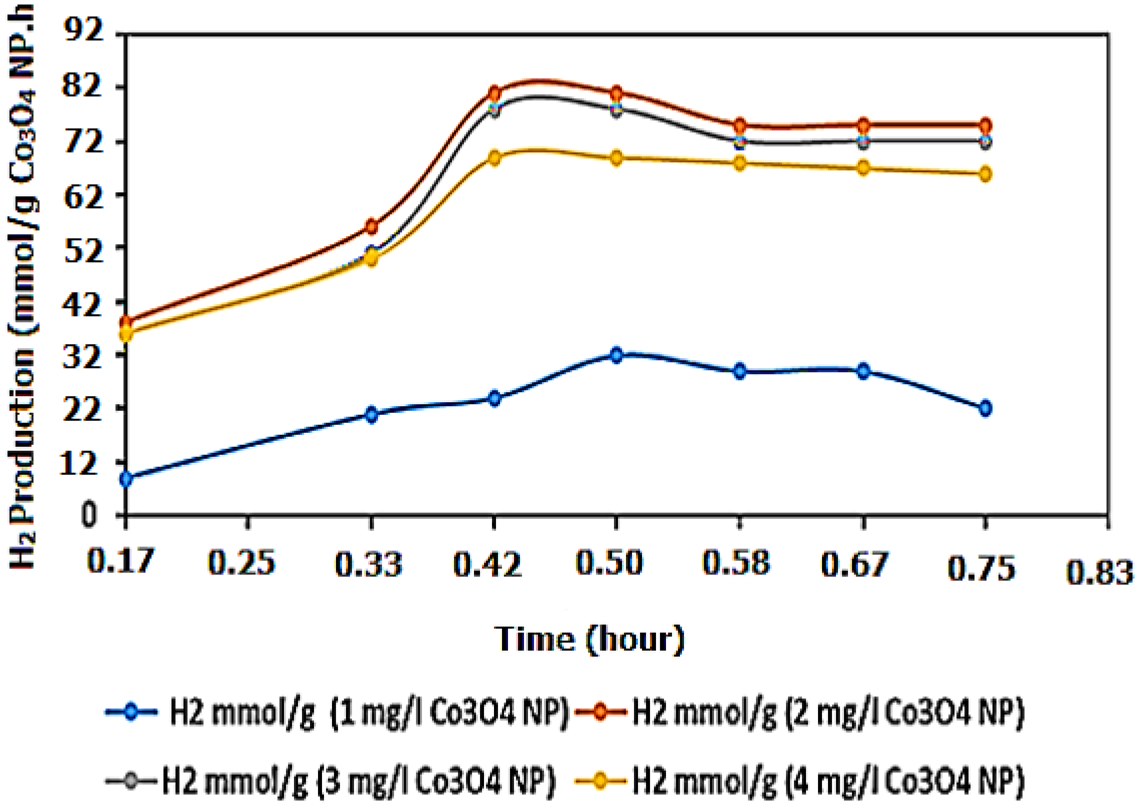

Figure 13. (d) H_2 production in Polymethyl methacrylate (PMMA).

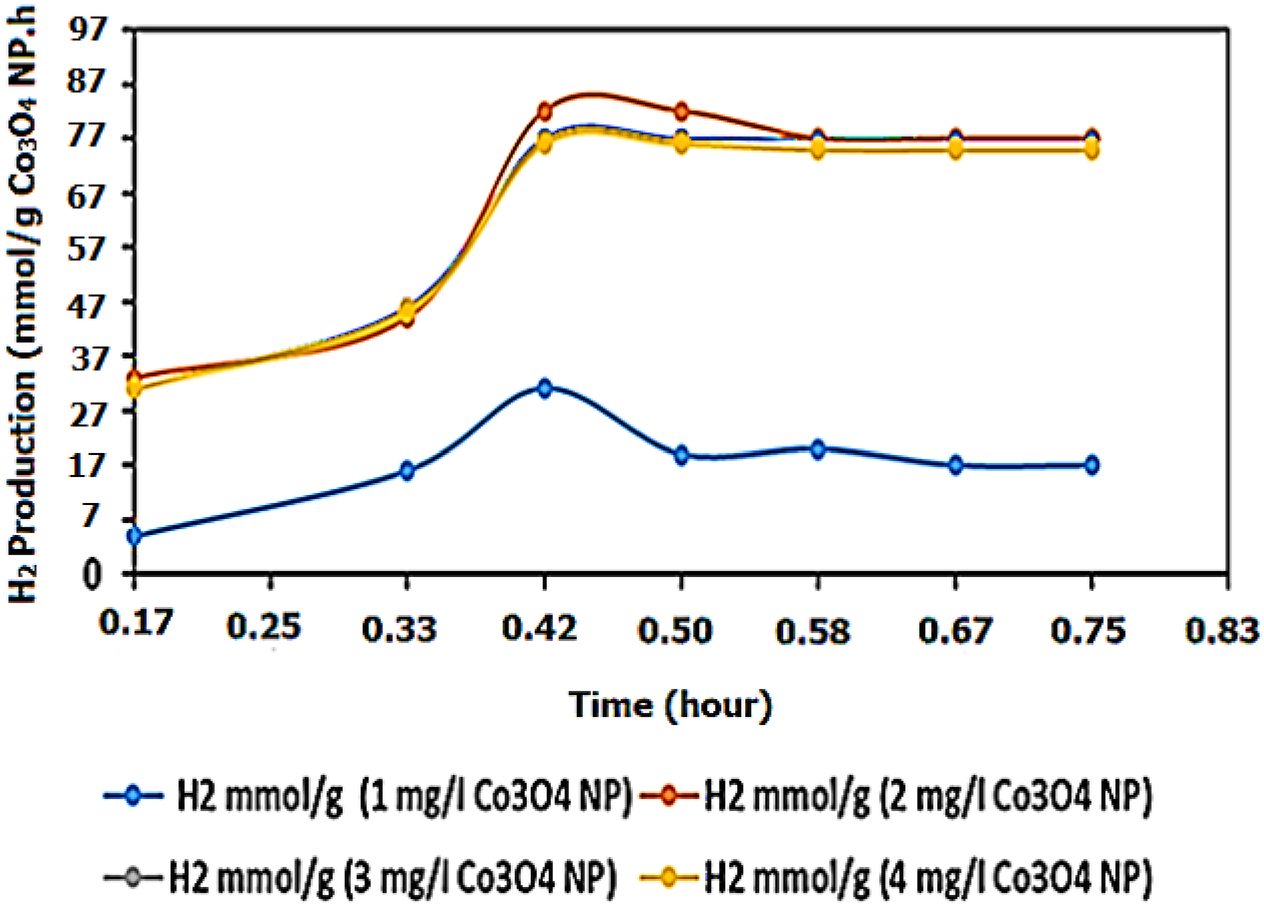

Figure 13. (e) H_2 production in Acrylates Copolymer (AC).

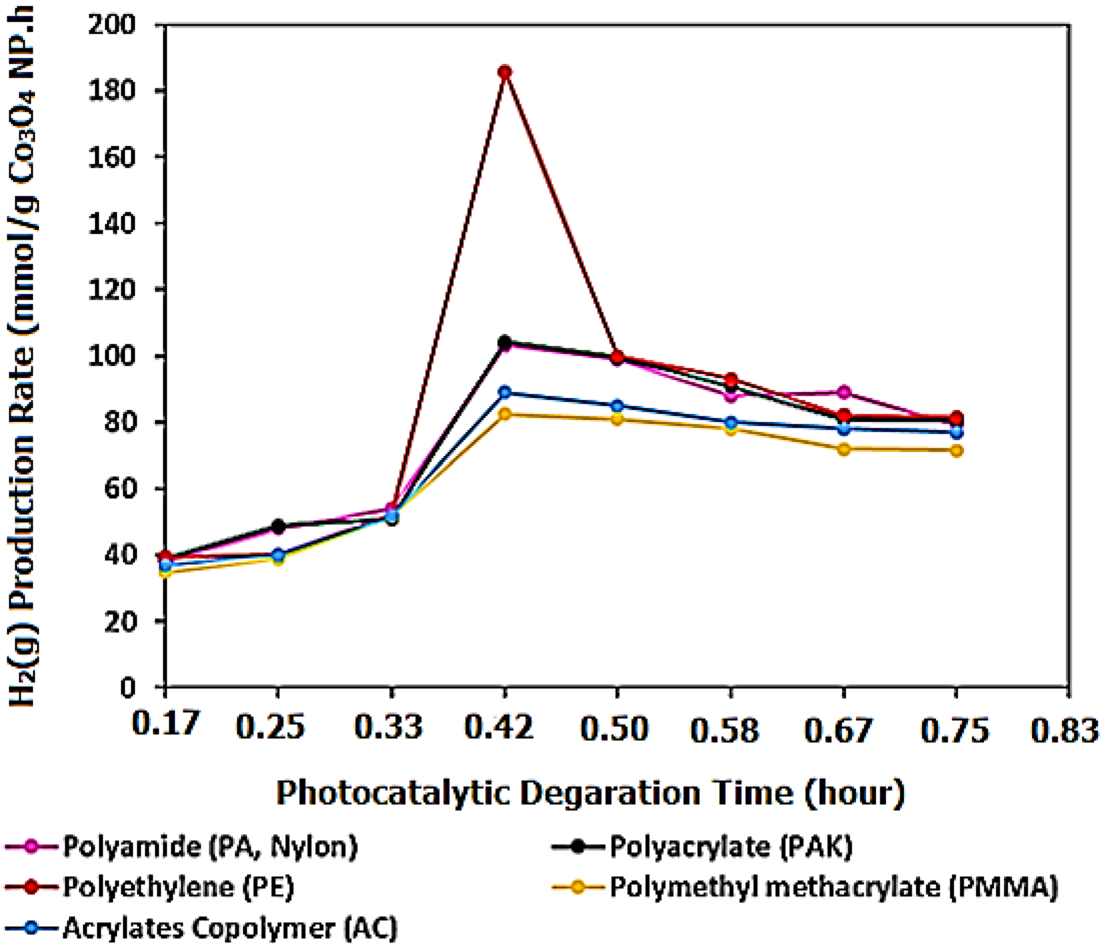

Figure 14. H_2 production rate for MPs [Polyamide (PA, Nylon), Polyacrylate (PAK), Polyethylene (PE), Polymethyl methacrylate (PMMA), Acrylates Copolymer (AC), respectively.

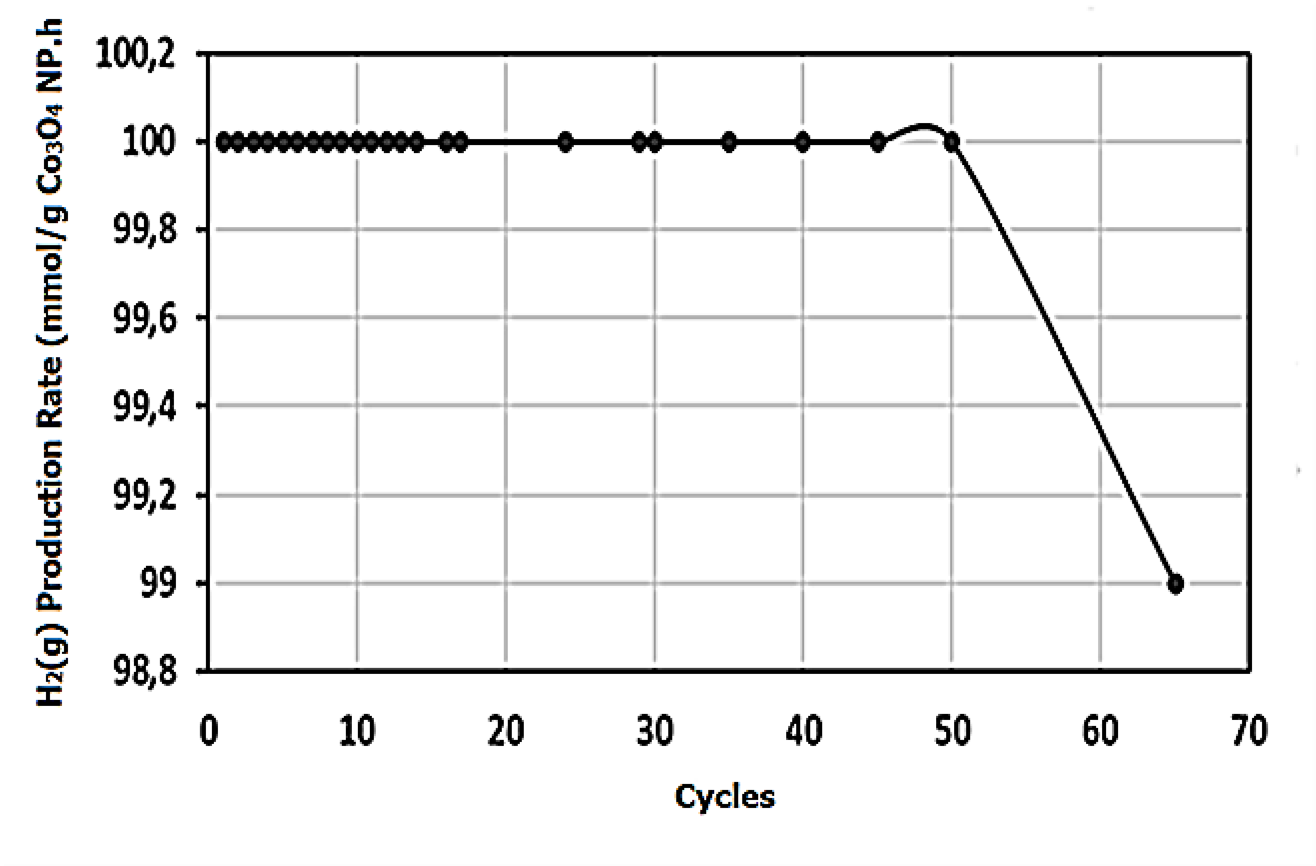

Figure 15. The reusability of Co_3O_4 NPs during 65 cycles.